Study of unintentional As incorporation into AlSb and interfacial layers within InAs/AlSb superlattices

by

Yunong Hu

A thesis
presented to the University of Waterloo
in fulfillment of the
thesis requirements for the degree of
Master of Science
in
Physics (Nanotechnology)

Waterloo, Ontario, Canada, 2019

©Yunong Hu 2019

Author's Declaration

I hereby declare that I am the sole author of this thesis. This is a true copy of the thesis, including any required final revisions, as accepted by my examiners.

I understand that my thesis may be made electronically available to the public.

Abstract

The InAs/AlSb material system has proven to be an excellent choice for high-performance mid-infrared quantum cascade lasers (QCLs). However, large localized strain may exist at the interfaces between indium arsenide (InAs) and aluminum antimonide (AlSb) layers grown by molecular beam epitaxy (MBE), likely influencing the electronic properties of InAs/AlSb based QCLs. In this work, an unintentional displacement of Sb by residual As flux incident on the wafer was studied by direct monitoring of such flux during a simulated MBE growth sequence and dynamical simulations of high resolution x-ray diffraction (HRXRD) data collected on InAs/AlSb periodic structures grown under similar conditions. The results revealed that the earlier reported predominant Al-As bonds detected at the InAs/AlSb interfaces can be attributed to a residual bypass As flux on the wafer after closing the As shutter. A considerable amount of As was incorporated into AlSb layers even when the As shutter was closed for As interruption during the barrier growth. The experiments revealed that under typical growth conditions, the barriers were converted to $AlAs_ySb_{1-y}$ instead of pure AlSb. The exact As content in the barriers was proportional to the effective As flux bypassing the closed shutter, thus depended on the particulars of the MBE system design and the exact As flux used for the growth of InAs wells. Moreover, instead of a strain-balanced interface, one monolayer of $(AlAs)_x(InSb)_{1-x}$ with more As than Sb were found at the InAs/AlSb interfaces.

Acknowledgements

Firstly, I would like to express my greatest gratitude and appreciation to my supervisor, Prof. Zbig Wasilewski, who has been encouraging, believing, and guiding me to discover my potentials and to give my best effort. I am grateful for him for always having faith in me and energizing me to add new layers on top of the boundary of my ability. The hours we spent together would always be good lessons for my life and for handling problems with positivity. I truly admire his decades of dedication, professionalism, and, most importantly, love to MBE. This work cannot be done without his vision, experience, and guidance.

I would also like to extend my thanks Man Chun Tam for patiently answering my questions, training me to operate the MBE system and procedures for characterizations, and helping me with the growths. I would not have learnt how to do MBE growths without his demonstrations. I would like to thank Christopher Deimert, Yinqiu Shi, Marc Jarkissoon, and Dr. Joseph Thomas for their assistance, intelligent ideas, and troubleshooting for all difficulties associated with the equipment. I also want to thank the current and past group members, Dr. Ho-Sung Kim, Ida Sadeghi, Hiroto Mizuno, and Chris Maxwell, for their support and fruitful discussions. I enjoyed working with all of these brilliant people.

I appreciate the University of Waterloo and the Department of Physics and Astronomy for making me a much better person than I thought throughout my four years as both undergraduate and graduate student. I believe my choice to study in Canada at the University of Waterloo is one of the wisest that I have ever made.

Last but not least, my sincere thanks to my family for all the support throughout my university life, and also to my friends for making my university life more colourful. I am truly grateful to my love, Ruoyan Fan, whom I met in the Department of Physics and Astronomy when we were both undergrads, for her endless support and inspiring discussions regarding mathematical aspects of this project.

Table of Contents

List of Figures vii

List of Tables ix

1 Introduction 1

2 Crystal Lattices 4

2.1 Unit Cell and Basic Lattice Types 4

2.2 Strain 7

3 Molecular Beam Epitaxy System 10

3.1 Load Lock, Preparation Module, and Cluster Tool 11

3.2 Growth Chamber 12

4 Characterization Techniques 17

4.1 In-situ Characterization Tools 17

4.1.1 Beam Flux Monitor 17

4.1.2 Integrated Spectral Pyrometry (ISP) 17

4.1.3 Reflection High Energy Electron Diffraction (RHEED) 19

4.2 Ex-situ Characterization Tools 20

4.2.1 Nomarski Differential Interference Contrast (DIC) Microscopy 20

4.2.2 High Resolution X-Ray Diffractometry 20

Bragg's Law and X-Ray Diffraction 20

4.2.3 Black-box Wafer Photography 21

5 InAs/AlSb Superlattices used in Quantum Cascade Lasers 23

5.1 Quantum Cascade Lasers (QCL) 23

5.2 InAs/AlSb based QCL 25

5.3 Strain in InAs/AlSb Multilayer Structures 27

6 Experimental Approach **30**

6.1 First-stage Mock Recipe Executions – As Flux Bypass the As Shutter 31

6.2 Second-stage Mock Recipe Executions – As Flux Temporal Dependence . . . 36

6.3 Experimental Setup of the Real Growths 41

7 Results and Analysis **47**

7.1 Growth Results 47

7.1.1 Nomarski Microscopy and Black-box Wafer Photography 47

7.1.2 HRXRD Scanning Result 50

7.2 XRD simulations 53

7.2.1 XRD fitting for As-induced strain 53

7.2.2 Possible Exponential Decay Pattern for incorporated As within AlSb Layers 59

8 Conclusion and Future Works **65**

Bibliography **68**

List of Figures

1.1 An Illustration of InSb-type and AlAs-type Interfaces 2

2.1 Lattice Point + Basis = Crystal Structure 4
2.2 Primitive Unit Cell 6
2.3 Cubic Lattice in 3D 6
2.4 The Zinc Blende Structure 7
2.5 Schematic of Tensile and Compressive Strain Regarding a Relaxed Layer . . 8

3.1 Schematic of a Veeco GEN 10 MBE System 10
3.2 Schematic of a Typical Growth Chamber 13
3.3 Schematic of a Beam Collimation Shield 14
3.4 Schematic of an Effusion Cell for Group III Elements 15
3.5 Schematic Illustration of the Surface Processes of the Impinging Atoms or Molecules 16

4.1 An Ion Gauge with a Filament, a Grid and a Collector 18
4.2 Schematic of the Formation of a RHEED Pattern 19
4.3 Bragg's Law Illustration 21
4.4 A typical HRXRD Configuration 22
4.5 The Black-box Wafer Photography Set Up 22

5.1 QCL Energy Band Diagram and Dispersion of Energy States 24
5.2 Lattice Constant vs. Band Gap for Common Semiconductor Materials. 26

6.1 Arsenic Flux at the Two BFM Positions under Different Valve and Shutter Settings in Logarithmic Scale 33
6.2 Fitted Exponential Decay Function when Closing the As Shutter with BFM Inserted for In Cell at Growth Temperature 37

6.3 Fitted Exponential Decay Function when Closing the As Shutter with BFM Inserted for In Cell at Idling Temperature 38
6.4 BFM Ion Gauge output for As_2 and As_4 with Valve Open/close 39
6.5 RHEED Patterns Taken During InAs Buffer Layer Growth for Sample C. . . 44

7.1 Nomarski Images for Sample A, B, and C 48
7.2 An Example of a Rough Area under Nomarski for Sample A 49
7.3 Comparison among Black Box Images of the Three Wafer Surfaces 50
7.4 XRD Scanning Results and Comparison among Sample A , B, C, and similated strain balanced InAs/AlSb structure. 51
7.5 XRD Dynamic Simulation Result for Sample A if Rxtra As only Existed at the Interfaces. 54
7.6 XRD Fitting for Sample A and the As Composition within the Superattice . 56
7.7 XRD Fitting for Sample B and the As Composition within the Superattice . 57
7.8 XRD Fitting for Sample C and the As Composition within the Superattice . 58
7.9 Fitting Result of As Exponential Decay Function for Closed As Shutter and Open As Valve, from Oscilloscope Data 60
7.10 Sample A XRD Simulation Result with Exponentially Decay As Content within AlSb Layers 62
7.11 Sample A XRD Simulation Result with Exponentially Decay As Content Comparing to an Abrupt Drop 63

8.1 Comparison of Pendellösung Fringes from XRD Simulation for Sample B. . . 67

List of Tables

2.1 Poisson Ratios and Vertical Lattice Constants for the Related Material . . . 9

6.1 BFM Readings at Inserted and Retracted Position for Three Different Valve and Shutter Configurations. 32
6.2 Tests for Influence on Flux when Changing Sb and As Valve Settings. 34
6.3 Structural Schematic for all Sample A, B, and C 42
6.4 Summary and Comparison for Sample A, B, and C 45

7.1 XRD simulation structure for Sample A 54
7.2 XRD simulation structure for Sample B 55
7.3 XRD simulation structure for Sample C 55
7.4 XRD Simulation Structure with Exponential Decay As Composition for Sample A 61

8.1 Summary of Growth and Fitting Results of Sample A, B, and C 66

Chapter 1

Introduction

InAs/AlSb superlattice structures have been a good candidate for high performance quantum cascade lasers (QCL). At low temperature, wavelengths as short as 2.63 – 2.65 μm can be obtained from an InAs/AlSb based QCL [1]. At room temperature, continuous-wave (CW) operation was reported with wavelength up to 15 μm [2], while the highest CW operating temperature of 320 K was demonstrated for devices lasing at 11 μm [3]. The advantage of InAs/AlSb structure is its very large conduction band offset up to 2.1 eV and a large Γ-L distance of 0.73 eV in InAs [4]. Moreover, InAs has a very small electron effective mass of 0.023 m_0, where m_0 is the rest mass of an electron. Therefore, the subband separation and optical gain observed is large for InAs based QCLs. However, due to no atoms in common between InAs and AlSb, only Al-As or In-Sb bonds can exist at the interface. Also, the lattice misfit between InAs and InSb is -6.6% and between InAs and AlAs is +6.9%, both are relatively large. As a result, large localized strain may exist at the interfaces; and the strain strongly influence the electronic properties of an InAs/AlSb based QCL. Recent transmission electron microscopy (TEM) studies indicated that Al-As bonds are more favorable at both interfaces, however, the interfacial structures can be complex, extending up to 3 monolayers (ML) [5]–[7]. An illustration of InSb-type and AlAs-type interface is plotted Figure 1.1. In this study, we further investigated the composition at the InAs/AlSb interfaces and the distribution of the strain across the barriers and the wells via high-resolution X-ray diffraction (HRXRD) experiments and dynamic X-ray diffrection (XRD) simulations.

By conducting the InAs/AlSb superlattice (SL) mock growth while monitoring the As flux directly, we found unintentional presence of As during the periods of AlSb barrier deposition. Consequently, the strain distribution in the SL structure changed significantly because

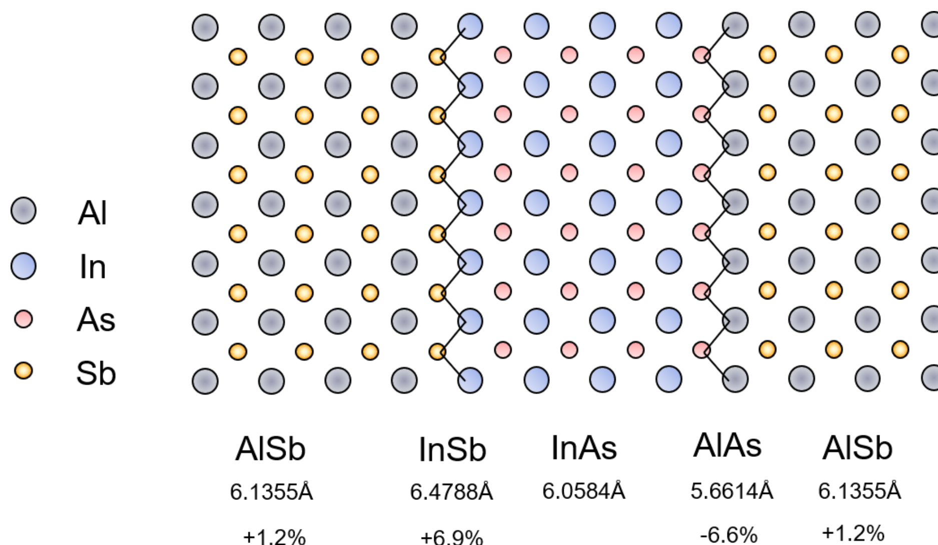

FIGURE 1.1: An illustration of InSb-type and AlAs type interfaces in an InAs/AlSb superlattice. Left interface: InSb; Right interface: AlAs

the incorporated As displaced some Sb and formed $AlAs_ySb_{1-y}$ layers in the barrier. The unintentional presence of As may be due to the limited capability of the As shutter to stop the As flux from entering into the chamber when the As shutter is closed. Even with a beam collimating aperture in place to reduce As bouncing effect and related temporal variations, the As pressure was still significant inside the chamber after the closure of the As shutter. Another reason that contributes to the As bouncing effect may be the non-unity sticking coefficient of the As to the wall of the growth chamber. At the time of writing this thesis, not much attention in the literature was given to the unintentional incorporation of As into the bulk of AlSb barriers during the deposition process. Such unintentional incorporation can be caused by a limited effectiveness of As shutters in molecular beam epitaxy (MBE) system.

In this series of experiments, we showed that the residual As pressure must be considered to accurately describe the strain in InAs/AlSb structures. There are two ways to interrupt the As beam and reduce the As pressure in the chamber: one is through only closing the As shutter in front of the As effusion cell, the other is through closing both the valve on the As cracker cell and the As shutter. However, closing As shutter would not completely prevent the As beam from entering the chamber because some As may still bounce around

the As cell port and bypass the As shutter. Moreover, closing the As valve along with closing As shutter is more effective in reducing the As flux in the chamber than closing As shutter alone. It is impractical to close the As valve during the switches of the superlattice layers, because the valve takes 1 to 2 seconds to open or close; and growing a single layer in the superlattices typically would take 5 to 40 seconds, depending on the layer thickness and the growth rate. To the best of our knowledge, for conventional InAs/AlSb superlattice growth, no literature mentioned the closing and re-open procedure of the As valve. Through our HRXRD analysis and dynamical XRD simulation, we found that excess As was present not only at the InAs/AlSb interfaces but also throughout the AlSb layers by displacing Sb, whenever the As valve was open throughout the entire growth process.

Chapter 2

Crystal Lattices

2.1 Unit Cell and Basic Lattice Types

A crystal is defined as a homogeneous solid with a highly ordered atomic arrangement in three dimensions. It is constructed by structural units, which consist of atoms or molecules with repetitions. A crystal structure is formed upon lattices where groups of atoms take the positions at each lattice point. Such added group of atom at each lattice point is called the basis [8]. In other words, a crystal structure is constructed with basis taking over each lattice points, as shown in Figure 2.1. All bases within one crystal have the same composition, orientation and arrangement.

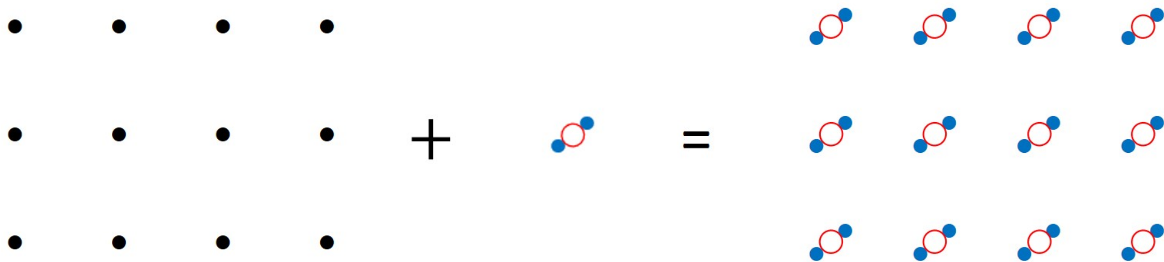

Figure 2.1: Adding basis to each lattice point forms crystal structure.
Left: lattice points; Centre: basis; Right: crystal structure.

In a three-dimensional coordinate system, we define a lattice translation operation by using a displacement described by translation vector

$$\vec{T} = u_1\vec{a}_1 + u_2\vec{a}_2 + u_3\vec{a}_3 \tag{2.1}$$

where $\vec{a_1}$, $\vec{a_2}$, $\vec{a_3}$ are fundamental translation vectors and u_2, u_2, u_3 are arbitrary integers. At any point $\vec{r'}$, the crystal looks the same as viewed from point $\vec{r}$ translated by vector $\vec{T}$

$$\vec{r'} = \vec{r} + u_1\vec{a}_1 + u_2\vec{a}_2 + u_3\vec{a}_3 \tag{2.2}$$

A lattice is described by the set of points $\vec{r'}$ which defined by all sets of u_1, u_2, and u_3. A primitive cell is constructed by primitive translation vectors $\vec{a_1}$, $\vec{a_2}$ and $\vec{a_3}$, with the smallest volume of $|\vec{a_1} \cdot \vec{a_2} \times \vec{a_3}|$ enclosed. This volume contains only one lattice point; hence the primitive cell is named a primitive unit cell [9]. For example, the lattice point at the intersection of four primitive unit cells is considered to contain only one-fourth of lattice point for each cell.

Therefore, the term "unit cell" is defined as a cell translated by multiples of the three primitive translation vectors $\vec{a_1}$, $\vec{a_2}$ and $\vec{a_3}$. The major difference between a primitive unit cell and a unit cell is that a primitive unit cell must contain one lattice point, while a unit cell may contain more. Unit cells that contain more lattice point are called nonprimitive cells. An example of primitive and nonprimitive unit cells is shown in Figure 2.2.

Expanding unit cells into three-dimension, a primitive unit cell contains one lattice point distributed to each of its eight corners. Each corner contains 1/8 of a lattice point. A primitive unit cell in three dimensions is indicated in Figure 2.3, where it is defined by three primitive translation unit vectors $\vec{a_1}$, $\vec{a_2}$ and $\vec{a_3}$, and they do not need to be orthogonal with each other. The angle between $\vec{a_2}$ and $\vec{a_3}$ is named α. Furthermore, β is defined as the angle between $\vec{a_1}$ and $\vec{a_3}$, while γ is defined as the angle between $\vec{a_1}$ and $\vec{a_2}$.

We mainly focus on III-V materials in the scope of this thesis. The III-V materials crystallize in the zinc blende crystal structure, as indicated in Fig 2.4. A zinc blende unit cell contains 8 atoms from two different main group. For instance, in Fig 2.4, if the yellow

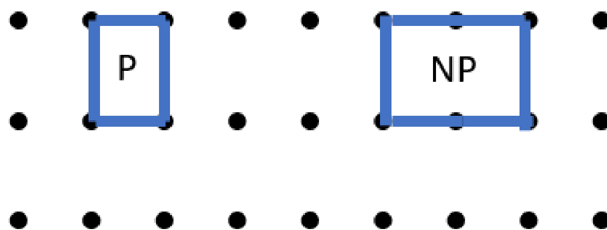

FIGURE 2.2: Examples of a primitive unit cell (left) and a nonprimitive unit cell (right). P = primitive unit cell; NP = nonprimitive unit cell.

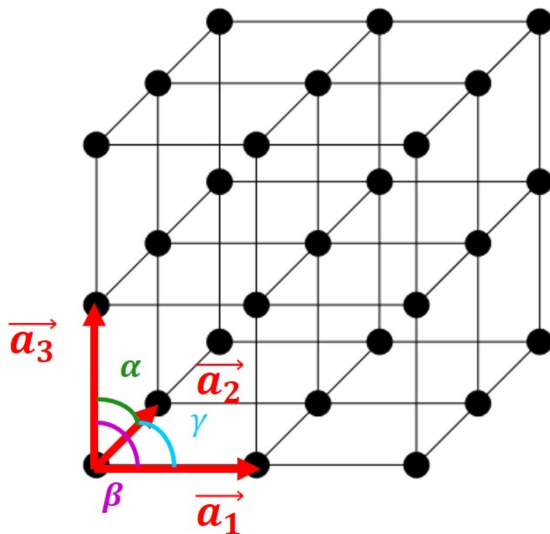

FIGURE 2.3: Example of a three-dimensional cubic lattice. A primitive unit cell is constructed by vectors $\vec{a_1}$,$\vec{a_2}$, and $\vec{a_3}$. α, β ,and γ are angles between each two vectors.

atoms represent group III atoms and the blue atoms represent group V atoms, two group III atoms are located at the corners and two located at the faces, while four group V atoms are located inside the unit cell. The zinc blende structure consists of two interpenetrating face centred cubic (FCC) sublattice. The two sublattices consists of different atom species and displace from each other by $(\frac{a}{4},\frac{a}{4},\frac{a}{4})$ along the cubic diagonal.

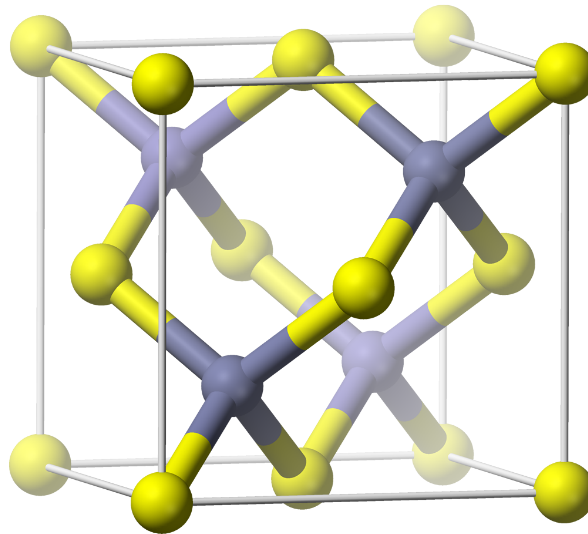

FIGURE 2.4: The zinc blende stucture of III-V semicontuctor materials.

2.2 Strain

Strain is produced at the interface between two crystal surfaces due to lattice mismatch during crystal growth. If two identical unreconstructed surfaces are brought into contact, the two surfaces can match because their surface orientation and lattice constant have no difference with the other. The dangling bonds match perfectly with the new bonds. Therefore, the two crystals are indistinguishable from each other [10]. If two different crystals are brought into contact, the positions of atoms and bonds would not match. This mismatch needs to be adjusted in order to form bonds between the two surfaces. Throughout the adjustment, the unit cells are distorted and their dimensions change. Strain is a measure of deformation representing the displacement between the dimension of the distorted unit cell

relative to its undistorted original dimension.

Strain can be tensile or compressive. Tensile strain is created when the lattice constant of the surface of the overlayer is smaller than the lattice constant of the layer below. The overlayer tends to expand to match the lattice constant of the layer below. In contrast, a conpressive strain occurs when the lattice constant of the overlayer is larger than that of the substrate. The overlayer tend to contract to match the lattice constant of the substrate. A schematic of tensile and compressive strain is illustrated in Fig. 2.5.

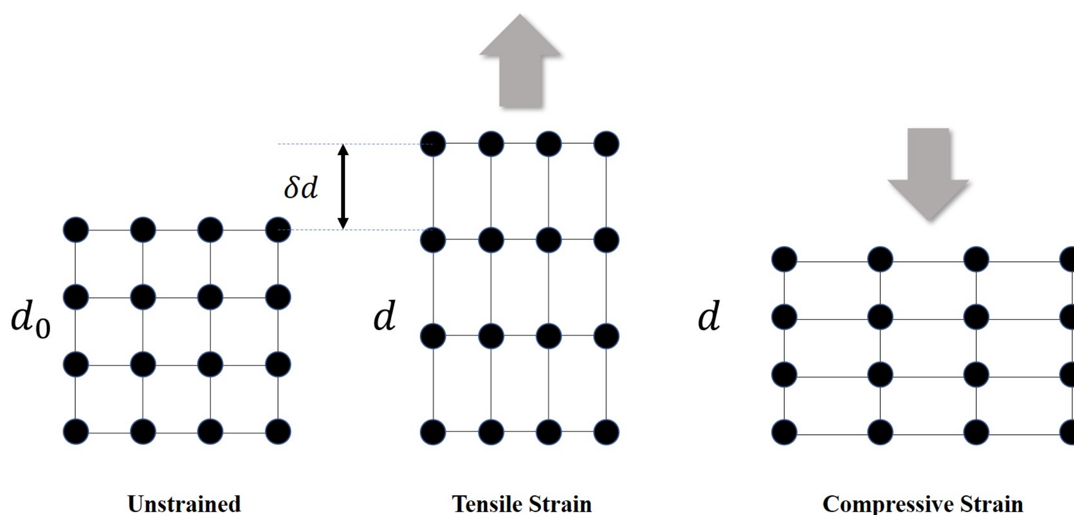

FIGURE 2.5: Schematic of tensile and compressive strain regarding a relaxed layer.

The strain can be defined in terms of the lattice parameters of the strained and the relaxed overlayer.

$$\varepsilon = \frac{\delta d}{d_0} = \frac{d - d_0}{d_0} \tag{2.3}$$

where d is the lattice constant of the strained layer and d_0 is the lattice constant of the relaxed layer.

If the layer is fully strained, the in-plane strain can be expressed as:

$$\varepsilon_x = \varepsilon_y = \frac{a_L^{\parallel} - a_L}{a_L} = \frac{a_S - a_L}{a_L} \tag{2.4}$$

where a_L is the lattice constant of the unstrained layer and a_S is the lattice constant of the substrate. The lattice constant of the in-plane strained layer should match that of the substrate. Also, the vertical lattice constant can be expanded (for compressive strain) or contracted (for tensile strain). The vertical strain ε_z can be expressed in terms of the in-plane strains ε_x ε_y and the Poisson ratio ν:

$$\varepsilon_z = -(\varepsilon_x + \varepsilon_y)\frac{\nu}{1-\nu} \tag{2.5}$$

The distorted vertical lattice constant $a_L^{\perp}$ can be expressed as [11]:

$$a_L^{\perp} = a_L \frac{1+\nu}{1-\nu} - a_S \frac{2\nu}{1-\nu} \tag{2.6}$$

The Poisson ratios and vertical lattice constants for the materials used in this project are tabulated below [11][12].

Material	Lattice Constant (Å)	Poisson Ratio ν	$a_L^{\perp}$ on InAs substrate
InAs	6.05840	0.352	6.05840
AlSb	6.13550	0.317	6.20707
AlAs	5.66143	0.325	5.27916
InSb	6.47880	0.353	6.93754

Table 2.1: Poisson ratios and vertical lattice constants for the related materials
[11][12]

Chapter 3

Molecular Beam Epitaxy System

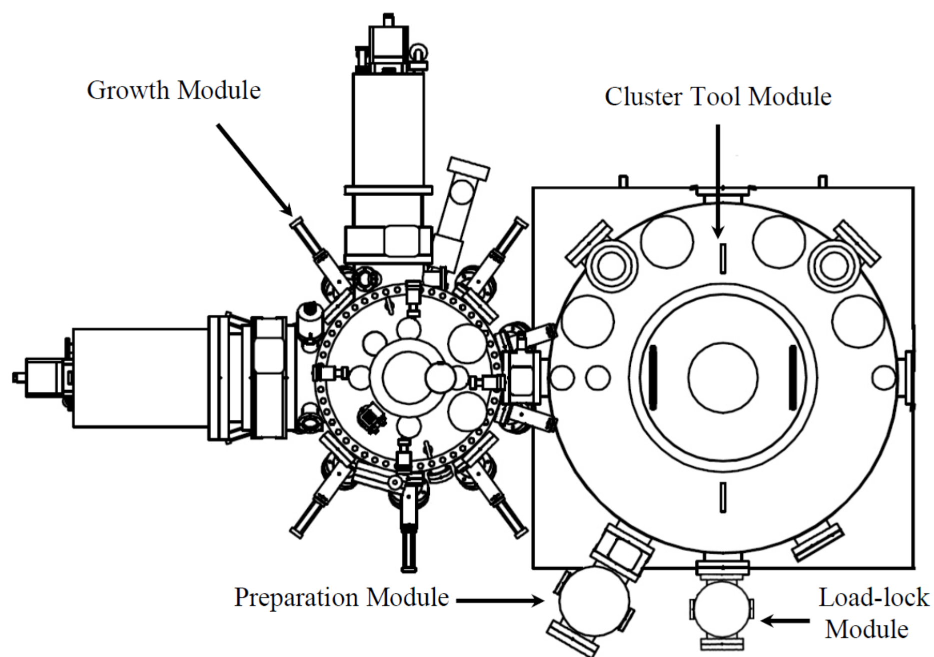

FIGURE 3.1: Schematic of a Veeco GEN 10 MBE System from a top-down view. An ion pump is vertically attached to the centre of the Cluster Tools Module. The four circle on the side of the CT are wafer storage positions, while the two concentric circles are glass viewports. A cryogenic pump and an ion pump are attached to the growth module. The parts sticking out are actuators for effusion cell shutters. Retrieved from [12]. Also seen in [13].

A Veeco GEN 10 MBE system is used for all the growths in our laboratory. A schematic of this MBE system is shown in Figure 3.1 [12]. The Veeco Gen 10 MBE system consists of a Load Lock module (LL), a Cluster Tool module (CT), a Preparation Module (PM), and a

Growth Module (GM). Effusion cells including As and Sb cracker cells are attached to the side-bottom of the GM. In this chapter, we introduce the modules following the sequence of wafer processing inside the system.

3.1 Load Lock, Preparation Module, and Cluster Tool

A Load Lock module serves as a wafer entrance to the ultra-high vacuum (UHV) system. It has a turbomolecular pump used for evacuating the LL after the LL is vented to atmospheric pressure; and then it maintains the vacuum condition inside. The typical working pressure inside our LL module is at the level of 10^{-8} Torr. After a substrate wafer is secured within a substrate holder outside of the system, the wafer can be manually transferred onto one of the eight shelves inside the LL at atmospheric pressure. The positions of those eight shelves are precisely controlled by a motor to elevate or descend vertically so that the selected shelf aligns with the opening port and the tunnel between LL and CT. A gate valve is used to separate the vacuum environment between LL and CT. A Convectron gauge is mounted near the venting/pumping port to measure the pressure on the pump side of the gate valve, while an ion gauge is used to monitor the module pressure. After loading the wafers into the LL and pumping it below 10^{-6} Torr, the temperature inside the LL chamber is raised to around 200 °C for the first step outgassing. This step is to evaporate any moisture left on the wafer and the wafer holder and other molecules that are volatile under 200 °C.

A Cluster Tool module serves as a wafer transferrer and storage. A robot arm with a substrate holder catcher can precisely transfer the wafer to any of the modules or parking positions within the CT. A total of 16 wafer parking positions are available inside the CT. Wafers that are grown, to be grown, and waiting to be prepared are parked at these positions. The typical pressure inside the CT is around 10^{-11} Torr. This pressure is maintained by an ion pump placed on the top of the CT.

After being picked up by the robot arm, the wafer is typically transferred to the Preparation Module from the LL or one of the storage locations for next-step outgassing. This is the last step before the wafer enters the Growth Module.

3.2 Growth Chamber

A Growth Module is a chamber that contains a substrate manipulator, effusion cells and shutters, in-situ characterization tools, and vacuum pumps. Internal to the growth chamber, there is a cryopanel which surrounds the manipulator and orifices of the effusion cells. Through the cyropanel, the liquid nitrogen (LN2) is circulated to cool the surfaces down and use the cooled surfaces to trap the contaminants. A schematic of an MBE growth chamber is shown in Figure 3.2. Before transferring a wafer into the GM, another outgassing procedure is conducted by heating up the substrate manipulator above growth temperature, and, meanwhile, heating up those cells to be used in the growth. Performing the GM outgassing is to minimize the contaminants remained on the substrate position, cells, and the chamber walls. After the substrate has been outgassed for around two hours in the PM module, the substrate manipulator temperature is cooled down to an idling temperature, while the cells are cooled down to growth temperatures. Subsequently, molecular fluxes for the cells are measured with a Beam Flux Monitor (BFM) to update the calibration of the the cell temperatures. Once the new growth temperatures are integrated into the pre-defined growth sequence (recipe), PM outgassed substrate can be transferred into the GM and placed in the manipulator. The growth recipe, prepared ahead of the process, is then transferred to a programmable logic controller (PLC) from Windows PC system, and the latter is controlling the recipe. The recipe includes ramping the temperatures for the substrates and effusion cells, operating cell shutters and cracker valves opening and closing, and substrate rotation.

Molecular beams are generated from heated elements contained in crucibles within the effusion cells. Four effusion cells are used in this project: a dual filament cell with 60cc pyrolitic boron nitride (PBN) conical crucible for Al, a 400g SUMO cell for In, a 500cc Marc V As valved cracker cell, and a 200cc Mark V corrosive series Sb valved cracker cell. For group III cells, the molecular beam flux exiting the cell is controlled by temperature of the elements only. A group III element within the cell is held in a PBN crucible, and surrounded by heater filaments. If the shutter is closed, the beam is blocked by the shutter and the vast majority of flux is prevented from entering the growth chamber for group III effusion cells. A schematic of a typical effusion cell is shown in Figure 3.4. The temperature of an In cell is controlled by two heater filaments; one at the tip, the other at the base of the element

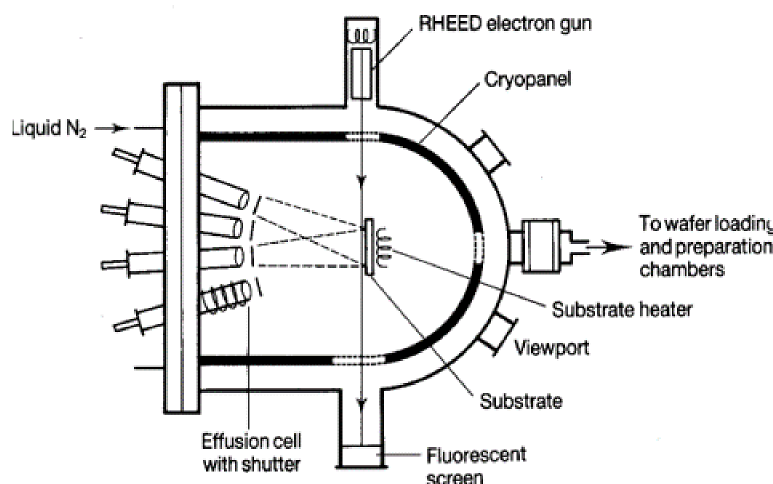

FIGURE 3.2: Schematic of a typical growth chamber. Retrieved from [14]

container. The Al cell we used is also dual-filament; however the top filament is disabled to keep the cell tip cooler, which prevents the Al from flowing out of the crucible. For As and Sb cracker cells, a cracking zone is used to crack tetramic group V elements into dimeric elements. For instance, the As_4 molecules can be cracked into two As_2 molecules. In this project, we primarily used As_2 for growth, and that requires the As cracking zone to be kept at 900 °C. As_4 has been used in mock growths in this project which requires the cracking zone temperature to be kept at 650 °C. The As cell has a large bulk evaporator which is kept at a constant temperature. For Sb cells, only one constant cracking temperature is used to generate Sb_2. The molecular flux of the group V elements is primarily controlled by the valve. Also, a shutter for group V cells enables/disables molecular beams entering into the growth chamber. In this project, we study the how As valve would affect the quality of the grown InAs/AlSb superlattice structure.

Both As and Sb cracker cell ports are equipped with an extra flux collimating shield (aperture) mounted on the LN2 cyropanel, effectively sealing off the port above the cell and the shutter. The purpose of such apertures is to minimize the exposure of the growth chamber to group V elements, leading to substantial reduction of material deposits on the cryoshroud. For As cells, such aperture is expected to reduce substantially so called shutter by-pass effect, where As molecules – as a result of non-unity sticking coefficient to the LN2

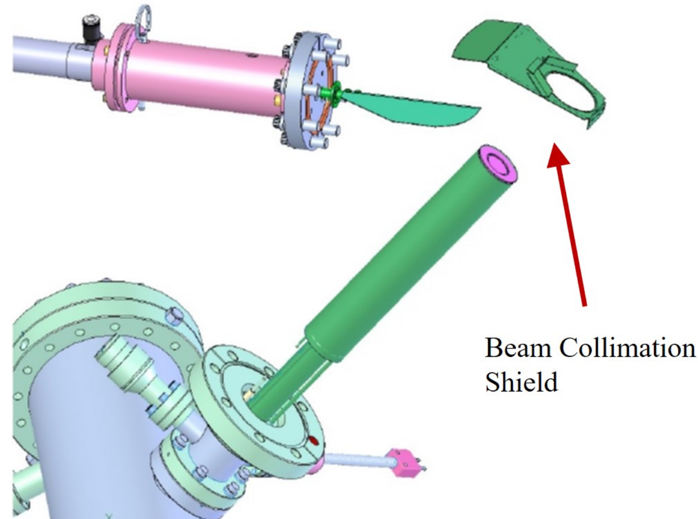

FIGURE 3.3: Schematic of a beam collimation shield in Veeco GEN10 MBE system. The beam collimating shield sits on the As cryopanel bay (not shown), effectively containing As flux there, with exception of the direct beam needed for the wafer growth.

shroud – would enter the growth chamber even in the presence of a closed shutter. Also, it significantly reduces the As bouncing around in the chamber and related temporal variations in As background pressure when closing and opening the As shutter and valve. A schematic of a beam collimation shield is shown in Fig 3.3.

A manipulator heats up the substrate before the molecular beams are engaged. A motor outside of the GM rotates the substrate during the growth. Prior to the start of the growth, we perform the oxide desorption procedure. For InAs wafer, the substrate is ramped to a higher temperature (500 °C) than the growth substrate temperature for 30 minutes. Meanwhile, we apply 2-3 times more As flux in the chamber than that of InAs growth. After the oxide desorption, the shutters of the cells are opened/closed under computer control, which allows molecular beams to reach the substrate and initiate the crystal growth.

Many physical surface processes take place on the substrate surface, including adsorption of impinging atoms, lattice incorporation of adsorbed atoms, surface migration and dissociation, and thermal desorption of the unincorporated atoms. The impinging atoms

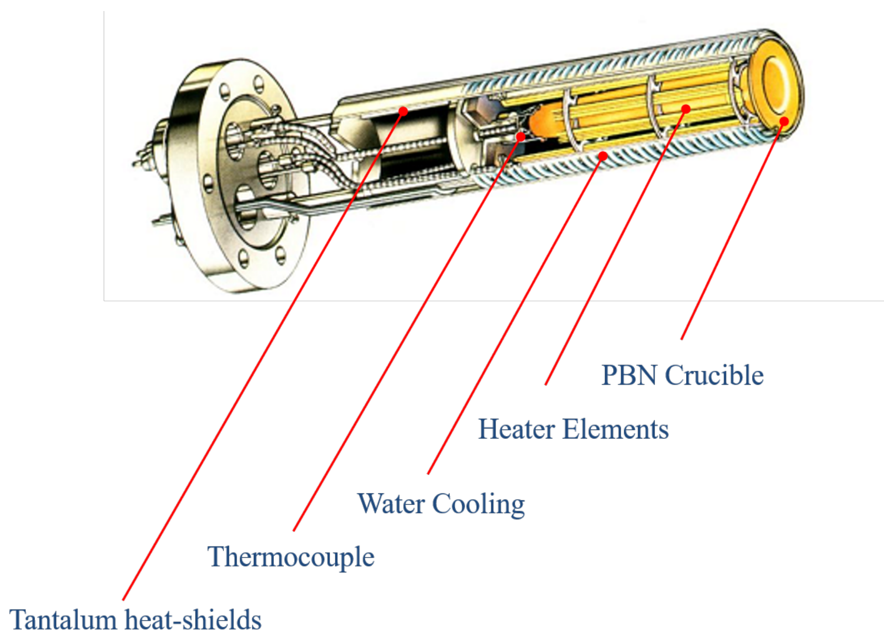

FIGURE 3.4: Schematic of a SUMO^{TM} effusion cell for Group III elements. Retrieved from [14]

firstly interact with atoms that occupy the substrate crystal site, and then adsorption of impinging atoms happens. Those adsorbed atoms continuously migrate along the surface; and some of those atoms are incorporated into the crystal lattice, forming islands with other impinging atoms or leaving the surface through thermal desorption. Figure 3.5 is a schematic illustration of these process happen simultaneously on the substrate surface [15][16].

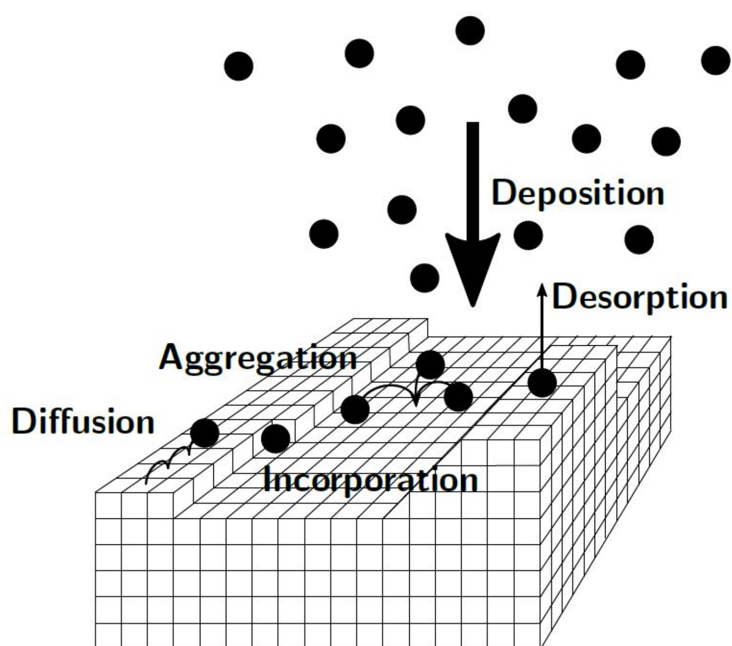

FIGURE 3.5: Schematic of the surface processes after atoms impinge onto the substrate surface. Lattice incorporation, surface diffusion, surface aggregation, and thermal desorption happen simultaneously on the surface. Retrieved from[15]. Also seen in [16].

Chapter 4

Characterization Techniques

4.1 In-situ Characterization Tools

4.1.1 Beam Flux Monitor

A beam flux monitor (BFM) is equipped with an ion gauge (IG) used to continuously monitor the atomic and molecular flux in the form of beam equivalent pressure (BEP). An ion gauge consists of a heating element that is an electron source, an electron-accelerating grid and a collector for detecting ionized particles formed by collisions between the accelerated electrons and the atoms inside the grid [17]. An illustration of an ion gauge is shown in Figure 4.1. For III-V systems, the electron source is usually made of thoria (ThO_2) coated iridium (Ir) filaments; this is because the thorium has a very low work function. The thoria coating lowers the work function for the electrons, so the electrons can leave without excessive filament heating. Therefore, it minimizes the outgasssing in the chamber. Our BFM is attached to a movable arm, which allows the BFM to move to the wafer position for flux measurements before and after the growths and also allows the BFM to continuously monitor the background pressure in the system at retracted position during the growth. The BFM plays an important role in flux measurements and cell temperature calibrations in this project.

4.1.2 Integrated Spectral Pyrometry (ISP)

For temperature monitoring during the growth of narrow band-gap materials such as InAs, an integrated spectral pyrometry (ISP) technique developed in our group is used

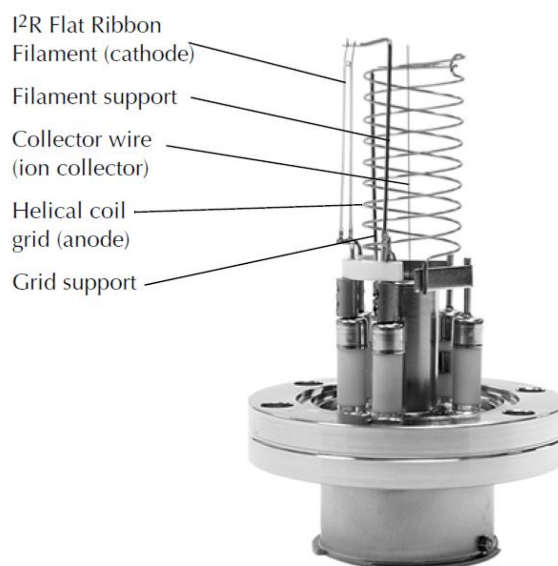

FIGURE 4.1: An ion gauge with a filament, a grid, and a collector. Adapted from [18]

[19]. Because narrow bandgap materials have lower congruent sublimation temperature and require lower growth temperatures than their wider bandgap counterparts, using single wavelength pyrometers may cause problems such as poor signal-to-noise ratio or high instability of temperature reading. The low signal-to-noise ratio is due to other infrared radiation sources in the system which bounce around the pyrometer and perturb the measurements. Moreover, the ISP relies on using a fiber optic coupled InGaAs array spectrometer to integrate the substrate thermal emission over a spectral range. Within this range, the substrate is opaque to the radiation from the manipulator heater, and the signal received is attributed to thermal radiation from the wafer. The spectral range of opacity for InAs is 900-1700 nm. This integration technique significantly improves the signal-to-noise ratio at low temperature for InAs/AlSb QCL growth on InAs substrate and vastly reduces the light interference effect which exists for single wavelength pyrometers. Therefore, temperature monitoring in this experiment is done by ISP technique. For calibration procedures, applications and details, readers are directed to Ref.[19].

4.1.3 Reflection High Energy Electron Diffraction (RHEED)

Reflection high energy electron diffraction (RHEED) can be applied as an in-situ technique for characterizing the surface of crystal samples [20]. The main elements of a RHEED gun are a high-energy electron gun and a fluorescent phosphorus screen. The electron gun generates a high-energy electron beam that impinges at a small angle (around 2°) relative to the surface of the wafer. The impinging beam is then diffracted by the surface of the wafer, creating diffraction pattern on the detector screen. RHEED can be used for identifying the surface reconstruction.A schematic of RHEED pattern generation is indicated in Figure 4.2.

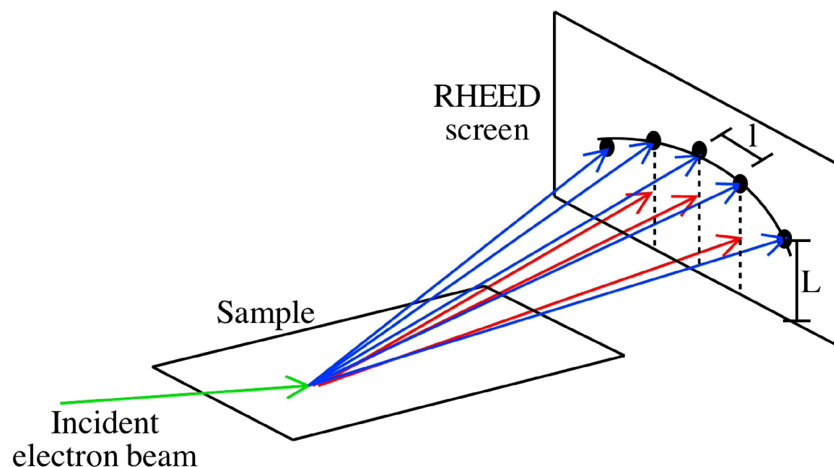

FIGURE 4.2: Schematic of the formation of a RHEED pattern. The spacing between the streaks is shown as l. Adapted from [21]

In the experiment related to this thesis, we used a RHEED system from Staib instruments, Inc. For this system, the electron acceleration voltage is ranging from 0.5 to 15 kV, and electron current from 0.01 to 100 μA. RHEED is used as a guide to optimizing growth conditions for the InAs-based QCLs in our group, and the structures grown in this project utilized the same conditions as other previously grown QCLs. Therefore, RHEED patterns in these series of experiments are used as criteria to check the surface quality of growing wafers.

4.2 Ex-situ Characterization Tools

4.2.1 Nomarski Differential Interference Contrast (DIC) Microscopy

The Nomarski differential interference contrast (DIC) microscopy was invented by Georges Nomarski in 1955 [22]. It can be used to analyze the defects grown on the surfaces of semiconductors. Also, it is routinely used in the semiconductor industry for assessing morphology of samples because of its vertical resolution in nanometer range while traditional optical microscopy is in micrometers [23]. In our Nomarski microscopy characterization of samples, a Nikon Optiphot-66 connected to a SPOT digital camera is used. Examples of images taken by Nomaski are shown in Figure 7.1 and Figure 7.2.

4.2.2 High Resolution X-Ray Diffractometry

Bragg's Law and X-Ray Diffraction

X-ray diffraction is a rapid analytical tool for characterizations of crystal structures. A filtered monochromatic light from the cathode ray tube is generated and directed onto the crystalline substance. The interaction between the incident monochromatic rays and the parallel crystalline planes creates constructive interference when Bragg's Law is satisfied. The incident rays impinge onto different crystal planes and are diffracted. A difference in optical path is therefore created and can be presented under Bragg's law [24]:

$$2d\sin\theta = n\lambda \tag{4.1}$$

where n is an integer, d is the spacing between two parallel crystal planes; the angle θ is the incidence angle and λ is the X-ray wavelength. The incidence angle θ is known as the Bragg angle when the Bragg's Law is fulfilled. Therefore, the lattice constant can be determined by measuring the Bragg angle for a known X-ray wavelength. The diffractometer used in our lab utilizes $K\alpha_1$ line of copper, 1.54056 Å, generated by bombarding copper targer by high-energy electrons. An illustration of X-ray diffraction on a crystal is shown in Figure 4.3.

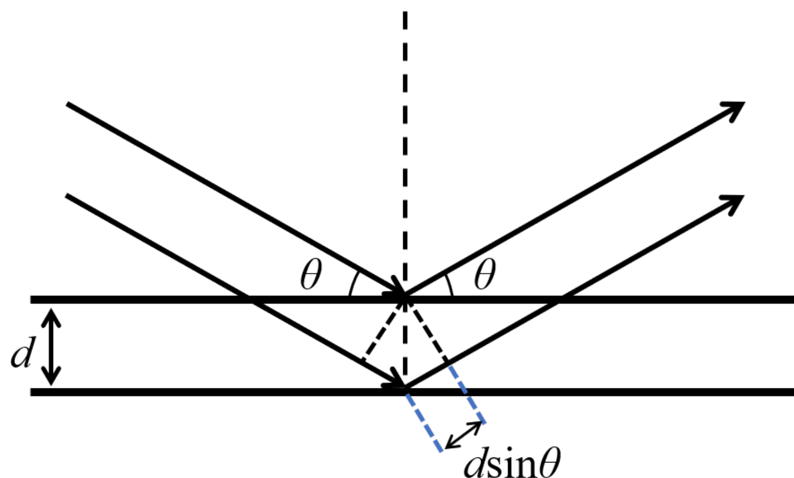

FIGURE 4.3: Impinging parallel X-rays beams interact with crystal substance. The difference in optical path is $d \sin \theta$.

For utilizing the X-ray diffraction, a configuration used in our lab is referred to as the High-Resolution X-ray Diffraction (HRXRD). The HRXRD apparatus used in this project is Jordan Valley QC3. Also, for the HRXRD scans in this project, the $\omega - 2\theta$ coupled scan is used. The ω is the incident angle between the crystal surface and the impinging X-ray, and the angle 2θ is the angle between the diffracted X-ray beam and the extension of the incident beam, as shown in Fig 4.4. The coupled scan is a plot of X-ray intensity vs. 2θ that varies 2θ and adjusts ω in order to make sure $\omega = \frac{1}{2} \times 2\theta + \text{offset}$ all the time.

4.2.3 Black-box Wafer Photography

The overall surface quality and defect locations for wafers can be checked directly using a system developed in our group based on a high-resolution digital single-lens reflex (DSLR) camera. The wafer is placed on top of a holder in the centre of a black box and a flashlight flares vertically above the wafer. Also, the camera is placed around 45° to the surface of the wafer, using a tripod. The beams from the flashlight undergo specular reflection at mirror-like smooth areas, while diffuse reflection is generated at defect points. Those defect points appear as bright dots in the image. The room light is switched off when taking the wafer photos.

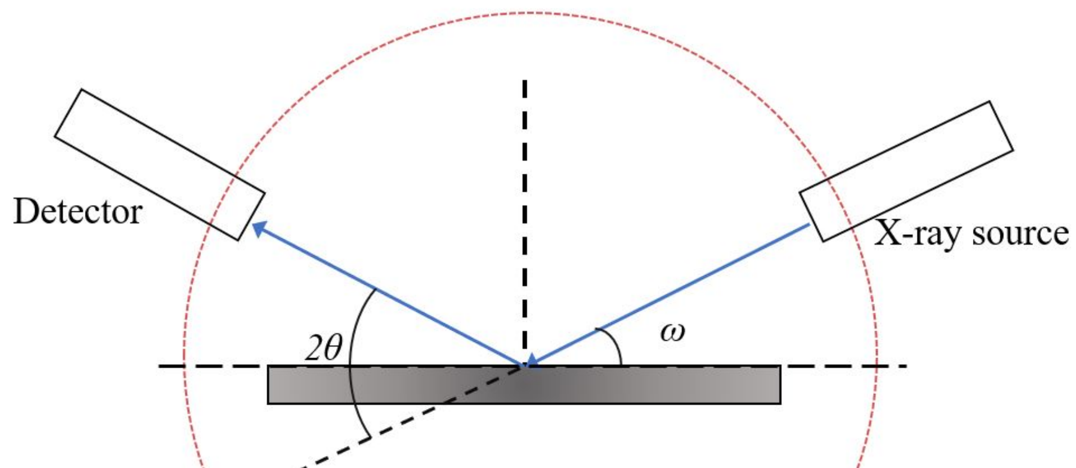

FIGURE 4.4: A typical HRXRD configuration for $\omega - 2\theta$ scan.

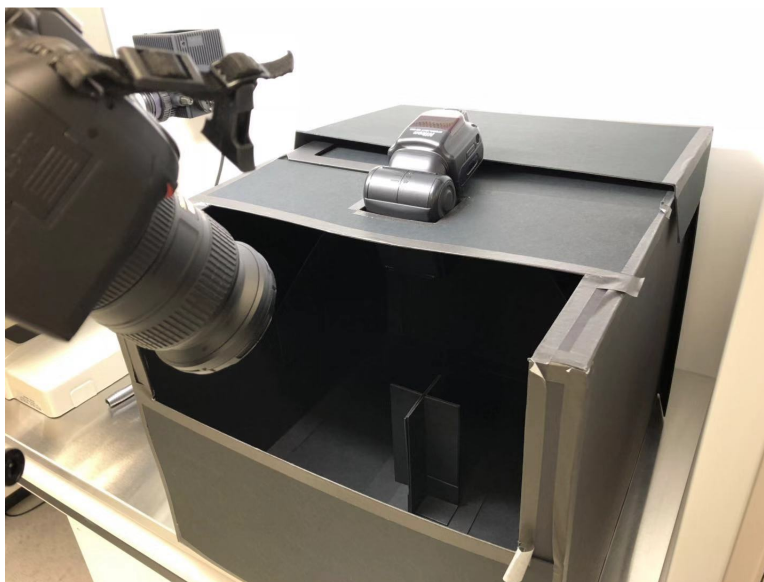

FIGURE 4.5: The set up of black-box wafer photography. A remotely controlled flashlight is right on top of the wafer position. The DSLR camera is angled around 45° from the normal of the wafer surface. The room is dark when taking the photo.

Chapter 5

InAs/AlSb Superlattices used in Quantum Cascade Lasers

5.1 Quantum Cascade Lasers (QCL)

The very first semiconductor laser was based on transitions between Landau levels biased in a strong magnetic field [25]. The laser was firstly purposed by Lax in 1960 before the invention of the diode laser. He assumed that observed transitions for bismuth using pulsed magnetic fields did not correspond to intraband cyclotron resonance, but were interband transitions [25].Two years later, the first diode laser was demonstrated by Hall et al [26]. The demonstration of diode laser drew the attention of global semiconductor community to bandgap lasers, and a race for inventing the first diode laser continuous-wave (CW) operation at room temperature was started. It was not until 1970 when the AlGaAs/GaAs heterostructure laser in continuous-wave operation at room temperature was demonstrated [27], and it was the mark of the development of diode lasers having reached maturity.

In the same year, Esaki and Tsu proposed in their seminal paper a concept of a superlattice, which formed an adjustable bandgap by repeated sequences of semiconductor layers [28]. One year later in 1971, Kazarinov and Suris proposed that under the external electric field, optical gain should be obtained for transitions between two-dimensional states in a superlattice [29].

Quantum cascade lasers were first demonstrated by J. Faist et al. at Bell Lab in 1994 [30]. Different from ordinary diode lasers, QCL is based on one type of carrier and electronic

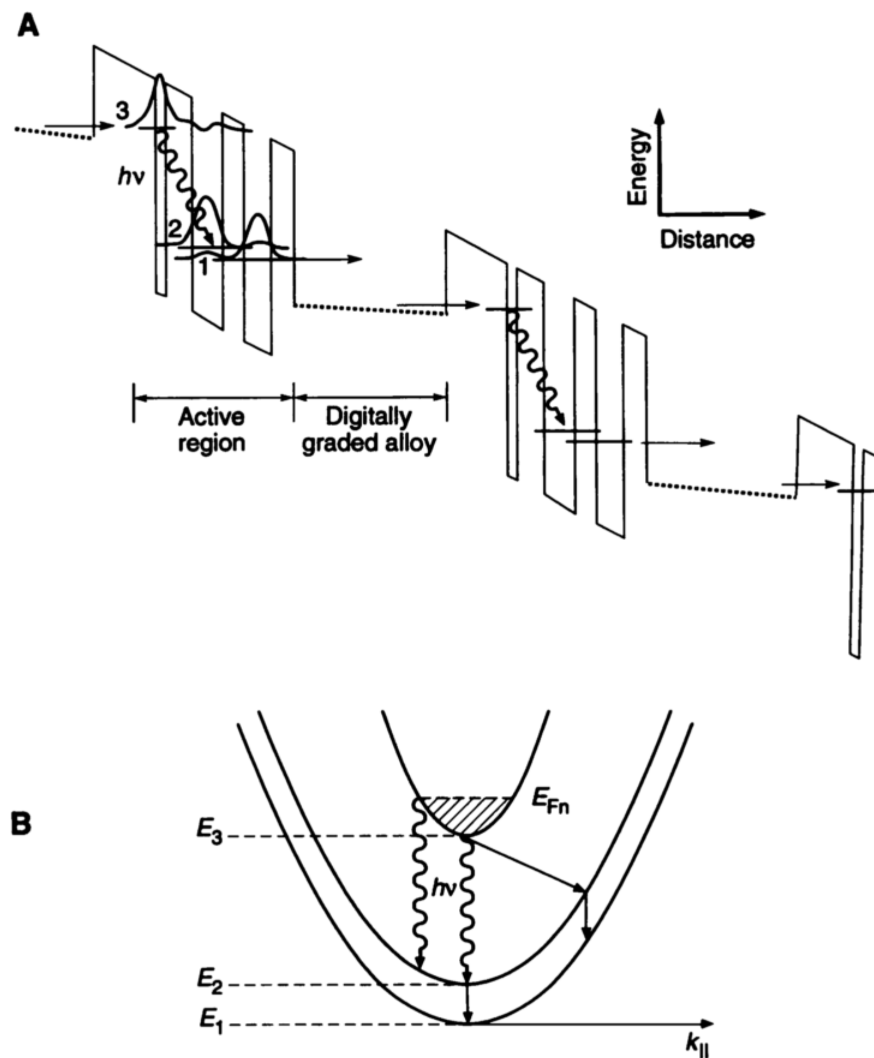

FIGURE 5.1: A. Conduction band energy diagram of the active region and injector from a 25-period section of a quantum cascade laser. B. Schematic of the dispersion of the n=1, 2 and 3 states parallel to the layers. Retrieved from [30]

transitions between the states of conduction bands. Those transitions are due to size quantization in semiconductor heterostructures. Therefore, the total combined density of states of transitions and the corresponding gain spectrum was symmetric and narrow. Their laser structure, which was $\mathrm{Al_{0.48}In_{0.52}As - Ga_{0.47}In_{0.53}As}$ heterojunction material system lattice matched to indium phosphite (InP), was grown by MBE. Through careful optimization of a sequence of 25 periods, each consisting of 3 quantum well active region and digitally graded alloy, electrical pumped laser action was achieved. The motion of electrons, parallel to the layers, as shown in Fig.5.1A, has plane wave-like energy dispersion. Also, the corresponding energy subbands are nearly parallel. Electrons are able to make transitions to a lower subband with photons emitted at a frequency, which corresponds to

$$h\nu = E_n - E_{n-1} \tag{5.1}$$

where h is Planck's constant. Faist et al. observed the emission for $n = 3$ to $n = 2$ transition, and their measured emission wavelength was $\lambda = 4.26\mu m$.

Later in 1996, J. Faist et al. extended the quantum cascade laser operation to higher temperature and a longer wavelength. They used similar GaInAs/AlInAs heterostructure active region lattice matched to an InP substrate. This QCL was able to operate above room temperature, and the wavelength range was extended to 11 μm [31]. Their work in 1998 expanded the QCL operation to a short wavelength of 3.5 μm at room temperature [32]. In 2004, J. Faist et al. demonstrated the quantum cascade lasers operating at terahertz region [33]. These devices operated at a cryogenic temperature up to 55K and had the wavelength ranging from 66 μm to 87 μm. Beck et al. in 2002 demonstrated their QCL CW operation up to 312K. They used high-reflection coatings on both facets of the heterostructure. The wavelength they obtained at 312K was $9.1\mu m$ [34].

5.2 InAs/AlSb based QCL

InGaAs/InAlAs grown lattice matched to InP and GaAs/AlGaAs grown on GaAs substrate were two of the most popular structures for QCLs in the past decade. The conduction band discontinuity for the lattice matched InGaAs/InAlAs on InP is $\Delta E_c = 520meV$ [35].

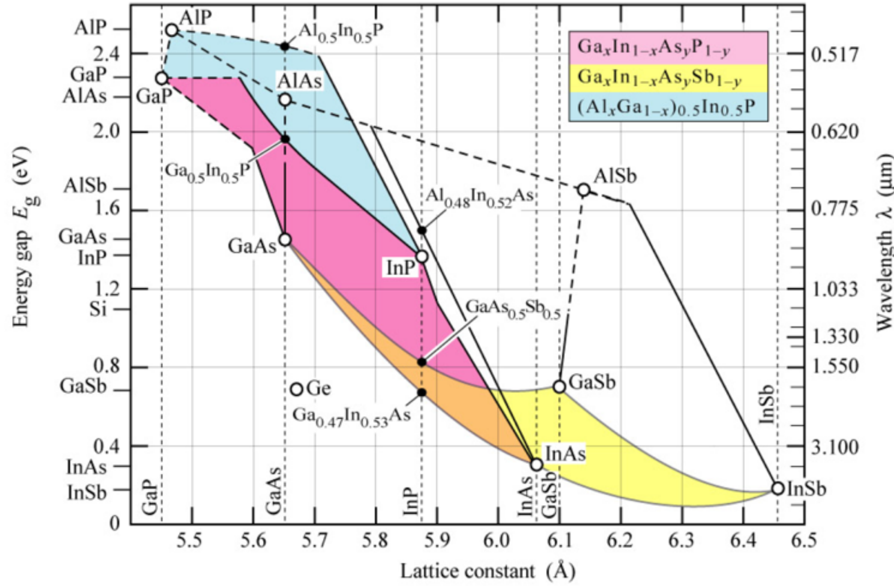

FIGURE 5.2: Lattice constant vs. band gap for common semiconductor materials. The conduction band offset between InAs and AlSb shown in graph is 1.35 eV. At Γ point, this band offset is up to 2.1 eV. The lattice constant of InAs was 6.058Å, and for AlSb is 6.135Å. The difference is 1.3% between them. Retrieved from [36].

In order to obtain a shorter wavelength, the conduction band discontinuity E_c had to be increased. The larger band discontinuity of 2.1 eV could be achieved by growing InAs/AlSb heterostructures, as shown in Fig5.2 [36]. Becker et al. in 2001 proposed that InAs/AlSb heterostructures grown on GaSb could be used for quantum cascade structure to obtain lasing wavelength of 3-5 μm [35]. Also, due to the small electron effective mass $m^* = 0.023m_0$ (m_0 is the rest mass of an electron) for InAs, a higher optical gain could be obtained for this structure [37]. However, the growth of InAs/AlSb material system had been challenging because there are no common atoms between the two materials [38], and the As-Sb exchanges at each interface need to be considered [39]. The lack of common atoms between the two materials leads to In-Sb or Al-As bonds at the interfaces. Moreover, those bonds induce high strain at each interface and affect the quality of grown QCL structure [4].

Dating back to 2003, Teisser et al. used a plasmonic waveguide with $n^+ -$ InAs cladding layers to obtain optical confinement for InAs/AlSb QCL. This QCL could operate at the

temperature of 220K and emit 6.7 μm wavelength [39]. One year later, their InAs/AlSb QCL was able to operate up to 300K, emitting near 4.5 μm with the help of high-performance waveguides. Breakthroughs for InAs/AlSb QCLs were continuously reported in the following years. In 2006, Baranov's group achieved QCL wavelengths ranging from 3.5 μm to 3.65 μm, corresponding to 140 K to 200K operation [40]. In 2007, they reported that their QCLs can emit the wavelength of 2.97 μm near room temperature, and the wavelength was reported as 2.75 μm at 80 K. This wavelength was the shortest one achieved for InAs/AlSb QCLs at that time [41]. In 2010, Baranov's group reduced carrier leakage into the L-valley of InAs with their special design. As a result, they were able to obtain wavelengths as short as 2.63 - 2.65 μm, operating at around 175 K [1]. Baranov's group reported that they achieved room temperature CW operation in InAs/AlSb based QCLs up to 15 μm [2] and 11 μm at 320 K [3], in 2016 and 2018, respectively. Those QCLs were the most recent InAs/AlSb reported before the writing of this thesis. Their performance were thought to be limited primarily by the interface scattering, which was a result from huge band offset of 2.1 eV and no atoms in common. Also, we demonstrated recently InAs/AlSb QCLs at 3.55 μm operating up to 350 K in pulse mode [42]. Therefore, for InAs/AlSb material systems, further investigation of the interfaces of the MBE growth structures was required for advancing QCL performance.

5.3 Strain in InAs/AlSb Multilayer Structures

For InAs/AlSb based QCLs, the AlSb barriers are just a couple of monolayers thick in order to achieve coupling between adjacent InAs quantum wells. Therefore, the precision of growing each layer should be at a sub-monolayer level [5]. The performance of InAs/AlSb based QCLs is therefore influenced by properties of interfaces between the layers. However, because of InAs and AlSb having no common atoms, Al-As bonds or In-Sb bonds necessarily exist in the interfacial zones. The problem is that AlAs and InSb both have large misfit with InAs, which is -6.6% and +6.9%, respectively. This may result in local distortions and affect the device property because of the loss of structural quality and the change of the band structure [43]. Moreover, because the structure is grown on the InAs substrate and AlSb has larger lattice constant, without providing some opposite strain, the stress will accumulate for thicker structures. Eventually, the accumulated stress may exceed the elastic

limit and generate dislocations. Therefore, the strain needs to be compensated to achieve the required InAs/AlSb superlattice (SL) thickness for Sb-based QCLs. Bauer et al. in 2010 inserted sub-monolayer AlAs layers to compensate the strain when using arsenic molecules in tetrameric As_4 form because of the reduced chemical reactivity of As_4 compared to As_2. They also applied As_2 to ensure a good ratio of interfacial Al-As and In-Sb bonds at the heterointerfaces to achieve strain compensated InAs/AlSb superlattices [44].

Nicolai et al. in 2014 investigated the strain at InAs/AlSb interface with high-resolution transmission electron microscopy (TEM) and scanning transmission electron microscopy (STEM). They demonstrated that compressive strains of AlSb grown on InAs could be compensated by AlAs-rich interfaces. Meanwhile, the tensile strain produced by InAs grown on AlSb could be compensated by forming InSb-rich interfaces. The reason for the formation of ultrathin interfacial layers was beyond the previous understanding that InAs and AlSb have no atoms in common. The fact that InAs and AlSb have no atoms in common was not sufficient to explain why ultrathin interfacial layers were formed. The lattice distortion examined in their research was different from the distortion due expected from the average mismatch between InAs and AlSb [5].

In 2015, Nicolai et al. investigated the formation of strained interfaces of AlSb/InAs. They identified a range of chemical composition of the strained interface, which was any quaternary limited by AlAs, $Al_{0.5}In_{0.5}As$, $AlAs_{0.16}Sb_{0.84}$, and $Al_{0.17}In_{0.83}As_{0.26}Sb_{0.74}$. The exact composition of the interfaces could not be derived from their analysis. However, they showed that the interfaces were Al-rich in character [6]. They also showed that Al-As bonds were most likely to appear on both InAs on AlSb interfaces and AlSb on InAs interfaces. Additionally, it was proposed that Al-As type interface is more favored because of its high thermal stability and bond energy. Later in 2016, Claveau et al. from A. Ponchet's group studied the InAs/AlSb interface elastic strain properties using Density Functional Theory (DFT). Their calculations of strain via DFT agreed with the prediction of structures with predominately Al-As interfaces [45].

In 2016, A. Ponchet's group cooperated with Baranov's group to investigate the extent of InAs/AlSb interfaces. They performed strain and elemental analysis by applying atomically

resolved Z-contrast images by high-angle annular dark-field imaging in a scanning transmission electron microscope (HAADF-STEM) [7]. They demonstrated a high content of Al-As bonds at the interface. A strain of -6% was obtained at the InAs/AlSb interfaces; it was of the same order of magnitude as they measured for perfect AlAs interfaces. However, they still could not accurately provide the exact value of strain because of abrupt strain variations [7].

In 2017, T. Zerderbauer et al. demonstrated that incorporation of Sb into $Al_xIn_{1-x}As_ySb_{1-y}$ was strongly dependent on temperature and growth rates [15]. Also, the quality of the material grown was highly correlated to the As pressure.

Chapter 6

Experimental Approach

In the experimental growths involving the As cell, we observed that it took a few seconds for As pressure to drop to the background pressure after shutter closure. Also, the arsenic background, which was higher after only closing the As shutter rather than closing both shutter and valve, may suggest that the As shutter mainly cut off the direct As beam from reaching the substrate, while some As may bypass the As shutter and still reach the substrate. In this chapter, the procedures and analyses of experimental growths are introduced to show that excess As content may be incorporated unintentionally at the InAs/AlSb interfaces and into AlSb layers, effectively forming $AlAs_ySb_{1-y}$ layers in the growth of InAs/AlSb superlattices. Due to the bouncing As in the chamber, we suspected that the excess As within the first AlSb monolayers may follow an exponential decay pattern or an abrupt drop; this needed to be verified from the analyses of the growths. Furthermore, there was limited research on As displacing Sb in AlSb layers. Also, there was no observed literature on the effect of the arsenic bypass in the chamber and its possible effect on the interfacial composition. Therefore, a gap in the literature existed in regards to the strain in the interface, attributed to the arsenic bypass, which resulted in unintentional As incorporation in AlSb layers. However, our experimental result and analysis in Chapter 6 and 7 supported the idea above.

6.1 First-stage Mock Recipe Executions – As Flux Bypass the As Shutter

Al-As bonds were suspected to be the primary cause of interfacial strains in InAs/AlSb heterostructures [5][6][7][45]. Excess As at the interfaces may cause Al-As bonds outnumber In-Sb bonds. Normally, the structure would be compressively strained because the lattice constant of AlSb is larger than that of InAs. As a result, the excess As may be beneficial for compensating the overall strain in the structure. Furthermore, previous research by XRD simulation from our group suggested that As displaced some of the Sb in AlSb layers. However, the location of the extra As was not clear. The extra As could be evenly distributed, forming $AlAs_ySb_{1-y}$/InAs, or located only at the interfaces, forming InAs/AlAs/AlSb with slightly less than 1 ML of AlAs [12].

We were trying to investigate why there was more As in InAs based QCLs than expected. Typically for such structures, switching between InAs and AlSb layers is done by closing one set of shutters while opening the other, without changing the setting for the cracker cells valves positions. Closed shutter is very effective in blocking Sb flux, since these molecules stick very effectively to all cold surfaces. However, this is not the case for arsenic molecules. Furthermore, during growths, the BFM was retracted. As a result, we were unable to know the corresponding molecular flux at substrate position during actual growths. Therefore, in order to evaluate the residual As flux reaching the substrate with the As valve closed, we positioned the BFM ion gauge at the front of the substrate manipulator. In this mock recipe execution, there was no need to grow an actual structure because only the data of beam equivalent pressure reading from BFM was needed. Hence, we did not use an InAs wafer as we normally do for growing InAs/AlSb heterostructure. Instead, a silicon wafer was placed at the substrate location as a dummy wafer.

Except for the wafer, we were trying to set the conditions for the mock recipe executions close to real InAs/AlSb growth. The substrate temperature was set to around 420 °C. The In and Al cell temperatures were adjusted to 766.8 °C and 1076.8 °C, respectively, to achieve a growth rate of 1Å/s for both InAs and AlSb. The dimeric form of As_2 was used by setting up the As cell cracking zone temperature to 900 °C. The Sb cell cracking zone temperature

was set to 950 °C and bulk evaporator temperature 530°C. The As (for As_2 only) and Sb bulk evaporator temperatures were fixed for all growths related to the topic of this thesis.

We measured three shutter-valve configurations, allowing for stabilization of the readings, with BFM inserted in front of the wafer position and BFM retracted. The readings were tabulated in Table 6.1 below:

BFM readings (Torr)	**As valve and shutter open**	**As valve and shutter closed**	**As valve open, shutter closed**
BFM inserted	4.05E-7	1.16E-9	4.52E-8
BFM retracted	2.7E-8	6.01E-10	2.90E-9

TABLE 6.1: BFM readings at inserted and retracted position for three different valve and shutter configurations. Plotted in Fig 6.1

For comparison and visualization, the As flux that BFM reads were plotted as a bar chart in Fig 6.1. Comparing the bar group 1 and 3 in the chart, we observed that closing the As shutter as we conventionally do in the growth decreases the As flux to around 11.2% of its flux during growth. Even with a beam collimating shield, which effectively reduces As bouncing in the chamber and As background pressure temporal variations, installed on the As cryopanel bay in our MBE system, such 11% shutter bypass As flux was still significant. Comparing the bar group 2 and 3, closing the As valve and shutter simultaneously was 40 times more effective in eliminating As from the chamber than closing the As shutter without closing the As valve. The flux reading after closing both the As shutter and valve was around 0.28% of its flux during growth. The flux readings when BFM retracted could not provide direct information for As flux at wafer position and it was listed for comparison only.

To conclude, there was still a significant amount (11.2%) of As flux remained at the substrate position if the As cracker valve was left open when the shutter was closed. The remaining As flux can be drastically reduced if As cracker valve was also closed.

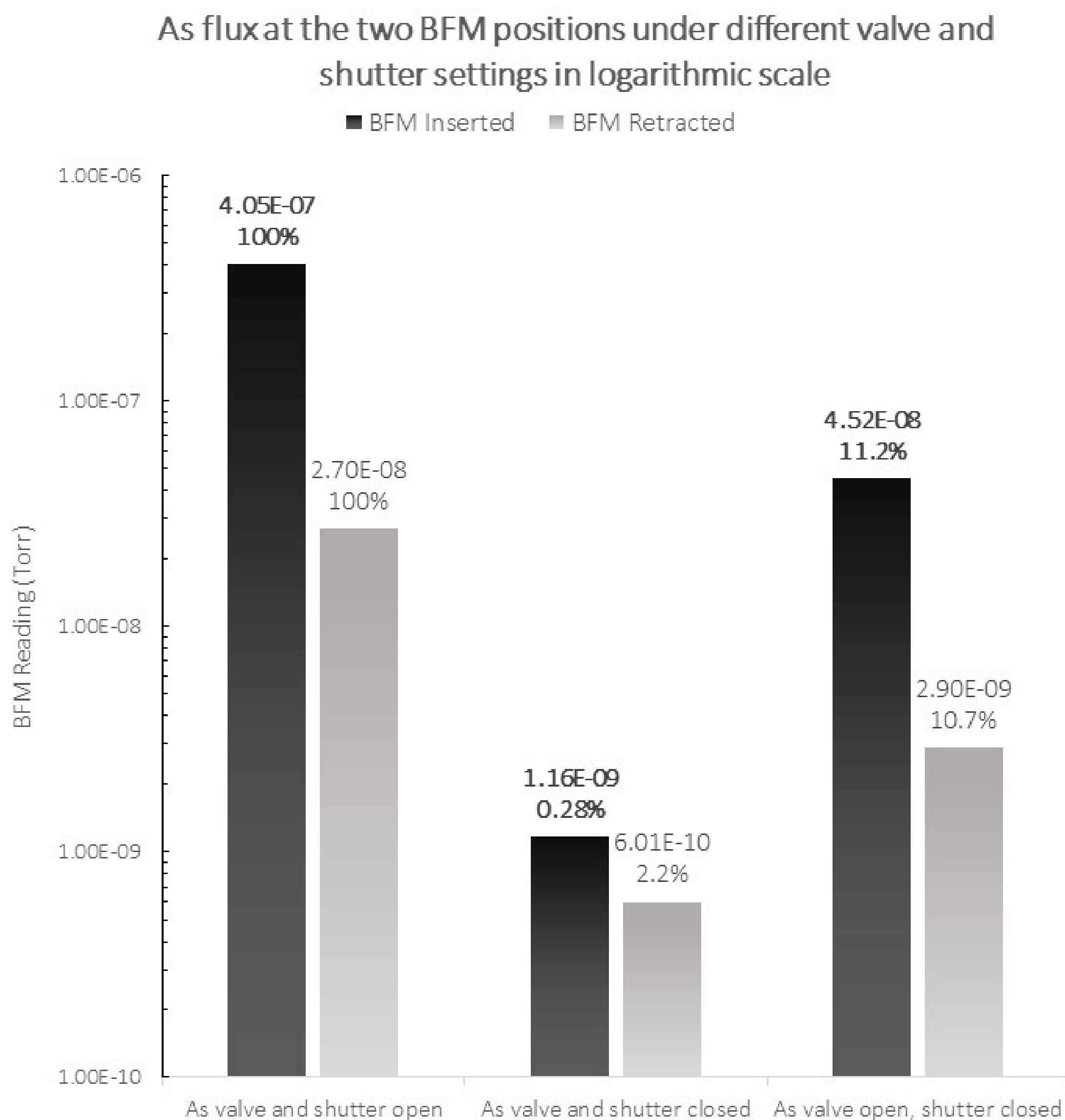

FIGURE 6.1: Arsenic flux at the two BFM positions under different valve and shutter settings in logarithmic scale. Black bars were BFM readings when BFM is inserted into the system near the growth position. Grey bars were BFM readings at retracted position

Conditions	**BFM readings when inserted (Torr)**
In shutter, As shutter & valve open. Sb shutter and valve closed	8.12E-7
In shutter, As shutter & valve open after closing Al, Sb shutters; Sb valve left open	8.02E-7
Al shutter, Sb shutter & valve open after closing In, As shutters; As valve left open	1.54E-6
Al shutter, Sb shutter & valve open after closing In, As shutters; As valve closed	1.51E-6
After closing Al shutter, Sb shutter & valve. None left open	6.78E-9

TABLE 6.2: Tests for influence on flux when changing Sb and As valve settings.

Before investigating whether leaving the As valve open when growing AlSb would affect the flux at substrate position, we needed to determine whether Sb shutter was effective in eliminating Sb flux in the chamber. Another mock recipe execution was conducted to answer these questions; and corresponding BFM values are recorded in the table below (Table 6.2):

In the first two rows from Table 6.2, the two flux values mainly consist of In and As flux. The readings showed that when Sb valve is left open but shutter closed, the BFM ion gauge reading was lower than closed Sb valve by 1.0E-8. There was no increment in BEP after Sb valve was open behind the closed Sb shutter. The difference in reading might result from the stabilization process of the As flux and was within the noise range of the BFM. Because the arsenic BEP detected by the BFM tends to rise slowly over time as the absorption and reflection/re-emission from the growth chamber surfaces approach the equilibrium, readings could be sightly different at different points of time. Also, Sb has tendency to act as adsorption pump that deposits on cold surfaces in the chamber wall and the ports where the cells are located. This could reduce the BFM reading. We may infer that leaving Sb valve open when growing InAs should not affect the combined In and As flux. Moreover, leaving Sb valve open was what we conventionally do for all growths involving alternations of As and Sb.

Comparing the third and fourth rows from Table 6.2, we observed a difference around 3E-8 Torr between the open As valve during AlSb growth and the closed valve, while the background (indicated in the last row) was only 6.78E-9 Torr which was small comparing to the difference. This difference may be attributed to the open As valve. If this was the case, As content may be incorporated into the interfacial monolayer, or even deeper throughout the AlSb layer. Therefore, we had reason to hypothesize that the extra strain at the interfaces of InAs/AlSb was due to extra As. Also, the extra As may be unintentionally incorporated into the AlSb layers, forming $AlAs_xSb_{1-x}$/InAs. The actual amount of As incorporation was yet to be determined in the following experiments. Furthermore, it was unclear that the unintentionally incorporated As was evenly distributed or followed some decay pattern.

For the first-stage mock recipe executions, when BFM was inserted, Al and Sb cell shutters were opened right after the As shutter was closed. Moreover, because the total flux of Al + Sb was larger than that of In + As, no As flux decay was observed. Therefore,

to further observe and verify the As flux decay pattern with BFM inserted, and to further investigate the influence of the As valve settings, several separate As flux tests were desired.

6.2 Second-stage Mock Recipe Executions – As Flux Temporal Dependence

We designed another series of mock recipe executions to investigate the As temporal behaviour after the As beam was interrupted at BFM inserted position. We intended to isolate As beam by using As cell only; however, this did not accurately represent the real growths where In and As cell were both at growth temperatures. Therefore, we need to test whether the In cell temperature will affect the As flux decay. Two As flux tests were performed using dimeric form As_2 at substrate temperature 420 °C, one with In cell at the growth temperature and the other with In cell at idling temperature. The comparison and curve fitting results were shown in Fig. 6.3 and Fig. 6.2.

From the fitting results, the simplified fitting function when In cell was at growth temperature yielded:

$$y = 5.03 \times 10^{-8} + 3.51 \times 10^{-7} \exp\left(-1.202x\right) \tag{6.1}$$

The simplified fitting function for As flux decay when In cell was at idling temperature yielded:

$$y = 4.35 \times 10^{-8} + 3.70 \times 10^{-7} \exp\left(-1.743x\right) \tag{6.2}$$

There is no significant difference between these two functions. The starting point and offset were within the range of BFM ion gauge reading fluctuation. The former function with In cell at growth temperature decays slightly slower than the latter function with In cell at idling temperature; however, this difference is not large enough to show that In cell at growth temperature helped to slow down the BFM ion gauge reading decay. Hence, we could not conclude from the comparison whether closed In cell temperature would affect the BFM ion gauge reading when the As shutter was open. However, to be consistent with the real growth conditions, we decided to keep In cell temperature at the growth temperature in the next several mock recipe executions.

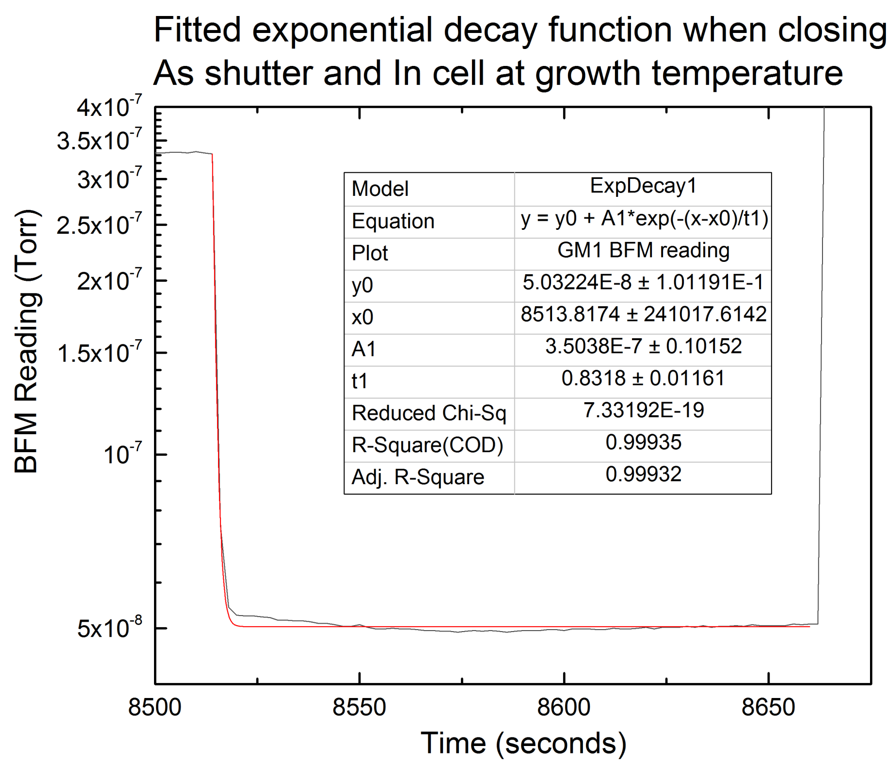

FIGURE 6.2: Fitted exponential decay function when closing the As shutter with BFM inserted for In cell at growth temperature

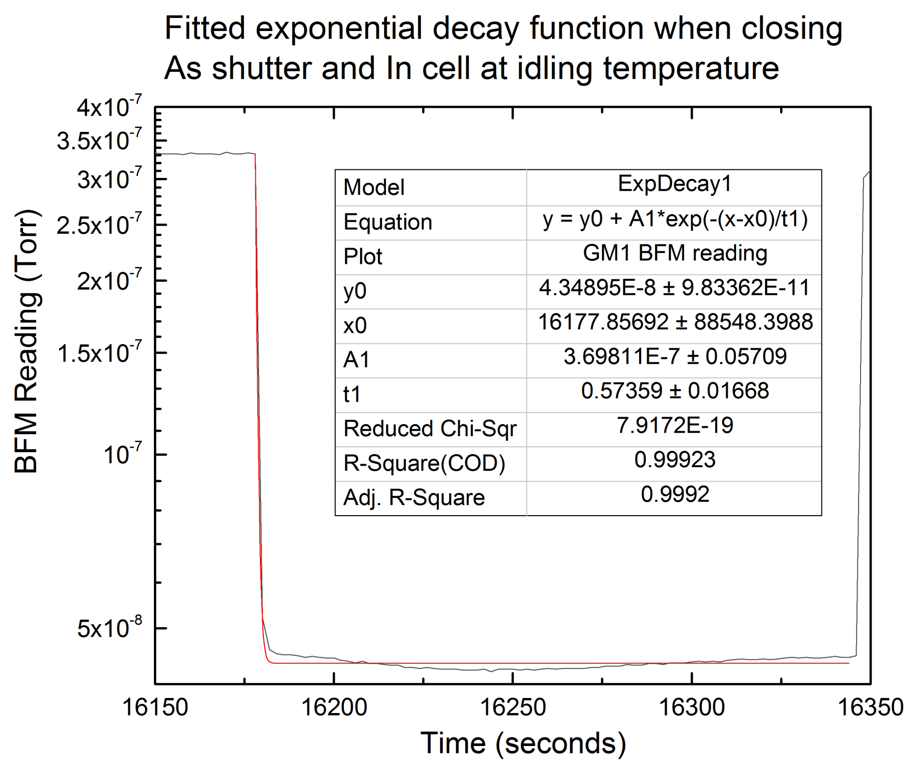

FIGURE 6.3: Fitted exponential decay function when closing the As shutter with BFM inserted for In cell at idling temperature

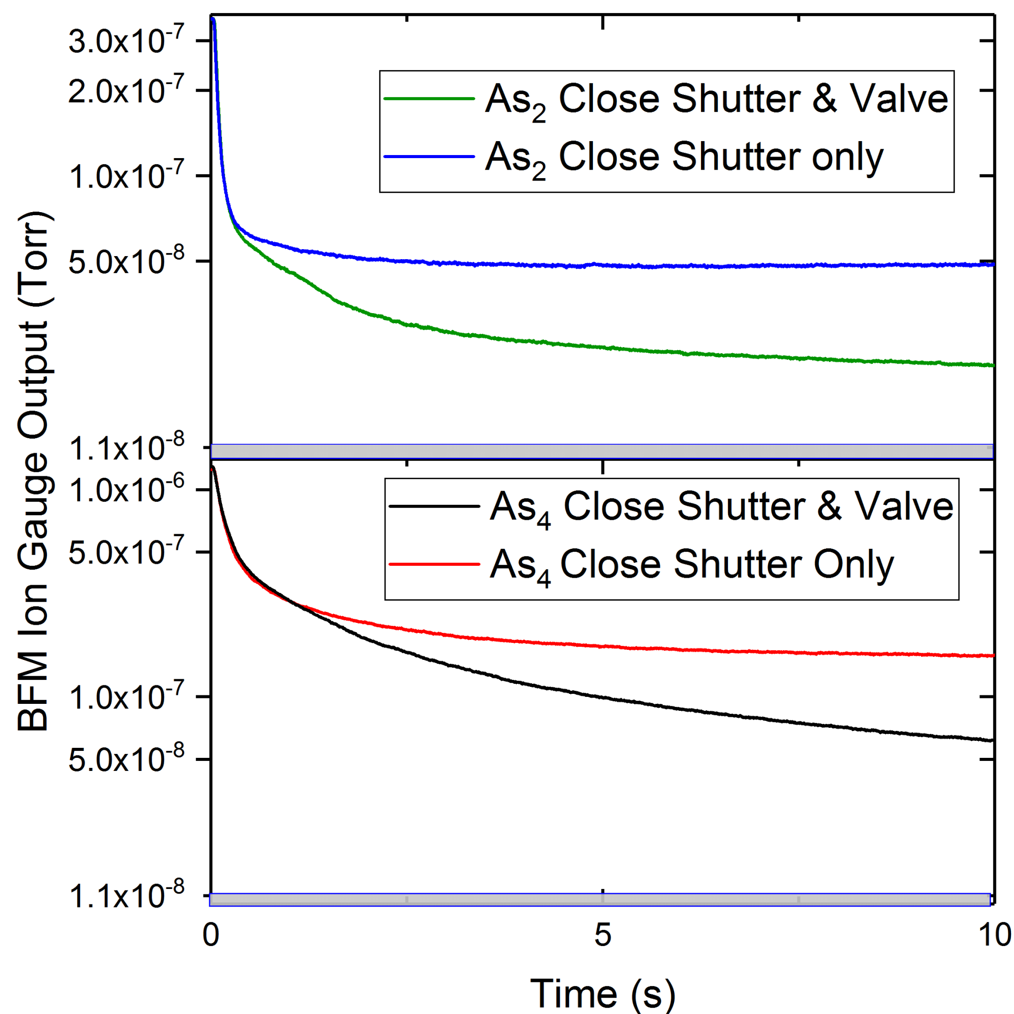

FIGURE 6.4: BFM ion gauge output for As_2 and As_4 with valve open/close plotted via semi-log graph. It takes about 1.4s for the As valve to be completely closed. The BFM background not related to arsenic is 1.1×10^{-8} Torr (shaded area). The shaded area is roughly 3% of As_2 growth flux. As_4 data in the lower pane is provided for comparison.

Another issue for fitting the curve was that the growth-monitoring logger takes one reading from BFM analog signal every 2 seconds; however, the most significant part of As exponential decay lasted less than 2 seconds. With the growth rate of 1Å/s, in two seconds, 2Å thick of AlSb could be grown; and this was roughly 2/3 of one monolayer of AlSb. The remaining As flux within that 2 seconds may be incorporated into the monolayer. Therefore, we need to investigate these two seconds of As temporal dependence. A sufficiently fast sampling rate was required for data acquisition. To solve this issue, we used a digital storage oscilloscope to convert the input analog signal into a digital recording of the amplitude of the signal at each sample time. The sampling interval has been improved to 2 ms. Observed exponential decay patterns had become much smoother during the mock recipe executions. We obtained four exponential decay patterns from dimeric As_2 and tetrameric As_4 after closing the As shutter with the As valve open and closed using the storage oscilloscope.

After mapping the voltage output of the BFM ion gauge controller to the pressure readings, we recorded the pressure reading versus time for the initial 10 seconds of the BEP at the substrate position. This was synchronized with the action of closing the As shutter only and also with the action of closing the As shutter and the valve simultaneously. For this experiment both As_2 and As_4 were tested; however, only As_2 was used for InAs well growth in this work. The results are shown in Fig 6.4.

After closing the As shutter and the associated initial rapid decline, the bypass As flux settled at a significantly lower value for As valve closed than opened. However, even with a closed As valve, the flux was still above the background at the end of the 10s interval. The rate of the initial flux decline for As_4 is clearly lower than that of As_2. This is expected in view of the higher reactivity of dimers compared to tetramers. It should be noted that the shutter closing action lasts less than 100 ms for both cases, however, the As valve takes about 1.4s to fully close from the settings used in the experiment. These two distinct actions, valve and shutter closures, are reflected in the temporal flux variations which is particularly clear for the case of As_2. These results show that during typical growth conditions, i.e. using As_2 and keeping As valve opened when growing AlSb, the rapid decline of As flux takes place well within the time needed to grow the first AlSb monolayer (about 3s), which is followed by a relatively steady unintentional As bypass flux. We can therefore expect that this will

result in an enrichment of InAs/AlSb interface with arsenic during QCL growth and then growth of AlAsSb ternary alloy instead of the intended AlSb binary. The exact levels of surplus arsenic at the interface and the following AlAsSb barrier cannot be assessed from this experiment alone. Indeed, the competition between As and Sb during AlAsSb growth is not well understood, other than it depends strongly on the exact growth conditions [15].

After two minutes when the background was stabilized, we measured the background to be 1.1 $\times 10^{-8}$ Torr, which is indicated in the figure as the shaded area. However, because this background was measured not long after the shutter closing, it tended to decrease slowly overtime. Eventually, after a few hours, the BEP was expected to decrease to the value corresponds to the background in 6.2 (6.78 $\times 10^{-9}$ Torr), or may eventually lower to the background in 6.1 (1.16 $\times 10^{-9}$ Torr). Nevertheless, the final background pressure might be different from time to time.

To further our understanding of the effect of the residual As flux has on nominal InAs/AlSb heterostructures, another set of experiments was performed, using the InAs/AlSb periodic design. By characterizing the strain distribution in the growth samples, the As distribution inside the barrier can be estimated.

6.3 Experimental Setup of the Real Growths

We had confirmed that the residual BEP for the case of the closed As valve and shutter (1.16 $\times 10^{-9}$ Torr) was roughly 2.6% compared to the residual pressure with the open As valve and closed shutter (4.52×10^{-8} Torr). Also, the latter residual pressure (4.52×10^{-8} Torr) was 11.2% of the As growth pressure (3.33×10^{-7} Torr), as previously stated in Fig 6.1. Therefore, there was a high probability that both the InAs/AlSb interface monolayers and the AlSb barrier were affected by the As valve settings. Hence, we designed three samples for MBE growth, which were labelled as Sample A, Sample B, and Sample C, respectively.

All of the three samples were grown on quarter 2-inch n+(S) InAs (100) wafers from Wafer Technology Ltd., and they were from the same wafer batch. The target structure was 200Å/150Å InAs/AlSb superlattices with 5 repeats grown on a 2000Å InAs buffer layer.

Since some of the contaminants were left on the surface after oxide desorption, growing a 2000Å buffer layer should effectively bury the contaminants and smooth out the layer surface after the oxide desportion. The layer dimensions and number of repeats were optimized to maximize information about the strain distribution in each period, which can be derived from dynamical simulations of the HRXRD data. The detailed schematic is listed below (the substrate is at the bottom):

Material	**Thickness**	**Repeat**
AlSb	150Å	5
InAs	200Å	
InAs	2000Å	1
InAs (001) undoped substrate	N/A	N/A

Table 6.3: Structual schematic for all Sample A, B, and C

The three samples were grown at nominally identical growth conditions, other than the arsenic valve setting during AlSb deposition. The substrate temperature was set to 420°C, which was monitored precisely by the integrated spectral pyrometry (ISP). The growth rate for both InAs buffer layer and InAs and AlSb superlattice was 1Å/s. Also, to ensure that the growth of InAs is stoichiometric, the fluxes for As and Sb were both set at values giving V/III flux ratio of 2, where the ratio of 1 means the minimum group V flux ensuring group V rich surface reconstruction. After several measurements and calibration, the target As flux was obtained by setting the As valve to 82. In the growths of all three samples, the As valve was maintained at 82 when growing InAs layers, and it was varied only during the AlSb layers deposition.

For Sample A, the As valve was left open during the growth of AlSb layers, as done in a conventional growth of InAs/AlSb QCL active layers. The activation of As flux was controlled by the As shutter only.

For Sample B, during the AlSb layers growths, the As valve setting was reduced to achieve an 80% As flux reduction. To find that valve setting prior to the growth, we initially calculated the 20% of the target As flux. Then, with an open As valve and shutter, we gradually reduced the As flux from target flux at the wafer position until 20% of target flux was reached. We recorded the corresponding As valve setting, which was 24 in our case. This value was the As valve setting we would reduce to when growing AlSb layers for Sample B. In other words, we maintained the As setting of 82 when growing InAs layers, reduced the As valve to 24 when growing AlSb layers, and then back to 82 again for InAs layers.

For Sample C, the As valve was fully closed during AlSb growth. For both Sample B and C, the As valve closing process was triggered simultaneously with the closure of the As shutter, while the valve opening process was triggered 1.5 seconds before the As shutter opening trigger. This ensured a fixed valve position during the entire InAs growth.

Before growing the buffer layer, the native oxide was desorbed from InAs substrate by annealing it at 500°C for 20 minutes under excess As flux, which was 2 to 3 times more than the As flux during growth (As valve setting 250 for these three growths). The use of excess As flux was to prevent the preferential As evaporation from the substrate and stabilizing the surface. Moreover, since the background pressure in the system monitored by the retracted BFM tended to rise over time for a given As flux, the time until the BFM ion gauge reading to be steady could be long. In these three growths, we explored a novel method to shorten the BEP stablization time under As flux measured by the retracted BFM. Instead of waiting for the BEP to rise from the background, we opened the As valve to a much higher setting for As pre-saturation. At this point, the BEP was still rising but it was much higher than the steady BEP that we desired. Then, the As valve setting was lowered to our growth setting (82) and the substrate temperature was ramped back to 420°C. With the valve lowered to the desired settings, the measured BEP dropped down to the desired level and remained at that pressure level. As a result, the desired As equilibrium pressure used for the growths was much quicker to reach.

After checking that both the desired substrate temperature and As flux were reached, the RHEED electron gun was engaged and the detector screen was opened. The substrate

was rotating at a speed of 1/3 revolutions per second.The RHEED camera were triggered at four different azimuths: 0°, 45°, 90°, and 180°, where 0° was aligned with (110) and 90° was aligned with ($\bar{1}$10). At this point, the growth of the buffer layer began. An As-rich surface reconstruction of (2×4) was observed for all the three samples. An example of RHEED pattern taken from Sample C InAs buffer layer growth is shown in Figure 6.5.

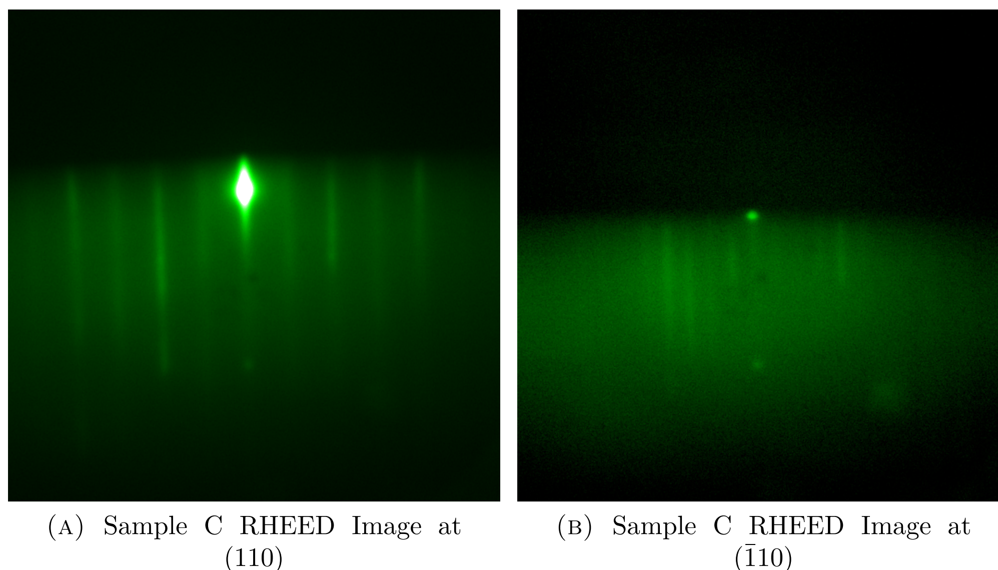

(A) Sample C RHEED Image at (110)

(B) Sample C RHEED Image at ($\bar{1}$10)

FIGURE 6.5: RHEED patterns taken during InAs buffer layer growth for Sample C. InAs(001)-(2×4) reconstruction was observed.

The substrate was cooled down after the growth process was completed. The In and Al fluxes were rechecked and the cells calibration parameters were updated from post-growth flux measurements. The Sb flux was also measured for the three samples to check for consistency before and after growths. A summary and comparison of Sample A, B, and C were tabulated below (Table 6.4):

After the fluxes of the cells were checked, temperatures of the cells were cooled down to idling temperature. Thereafter, the wafer could be removed from the GM and transferred to the LL for removal from the system. Further characterization including Normaski DIC

	Sample A	**Sample B**	**Sample C**
Key difference for interface growth after closing As shutter	As valve left open	As valve set to 20% of growth flux	As valve fully closed
As valve setting (shutter open - close)	82-82	82-24	82-0
BFM reading (retracted, Torr) for testing As flux	2.68 E-8	2.93 E-8	2.78 E-8
Sb BFM reading (Torr) before growth at extended position	9.89 E-7	9.77 E-7	9.86 E-7
Sb BFM reading (Torr) after growth at extended position	9.954 E-7	9.86 E-7	9.79 E-7

Table 6.4: Summary and comparison for Sample A, B, and C. BFM readings at retracted position for As during the growths are included. BFM readings at inserted position for Sb before and after the growths are also included.

microscopy, HRXRD, and black-box wafer imaging were done once the grown wafers have been retrieved from the MBE system.

Chapter 7

Results and Analysis

7.1 Growth Results

The growth results in this section are presented through images from Nomarski microscopy and black-box direct wafer photography for surface morphology examining. Structural characterization was done using High-resolution X-ray Diffraction.

7.1.1 Nomarski Microscopy and Black-box Wafer Photography

For most part of the three samples, Nomarski microscopy images presented satisfactory morphology. The number of defects per unit area was relatively low, and the surface under $\times 40$ objective magnification was very smooth. Several images were taken for all three samples, as shown in Fig 7.1. The images of Sample A and B were captured from the wafer centre while the images of Sample C were taken near the edge of the wafer. From the overall smooth surfaces, it can be inferred that the growth conditions were well optimized. However, we observed several areas of roughness for all the three samples. Those rough areas were located only at the corners of the cleaved quarter wafer. The surface roughness was confined to a circular area, and the morphology shifted from smooth to rough at the boundary of the circular area, as shown in Fig 7.2. A boundary dividing rough area and smooth area can be clearly seen in Fig 7.2. The roughness was most likely caused by a strong thermal gradient in the corner areas. We avoided the rough areas in HRXRD characterizations.

The black-box images of the three samples were taken with a DSLR camera. For all Sample A, B, and C, rough areas can be observed at the corners of the quarter-circle growth

(A) Sample A ×5

(B) Sample A ×40

(C) Sample B ×5

(D) Sample B ×40

(E) Sample C ×5

(F) Sample C ×40

FIGURE 7.1: Nomarski images for Sample A, B, and C at × 5 and × 40 magnifications

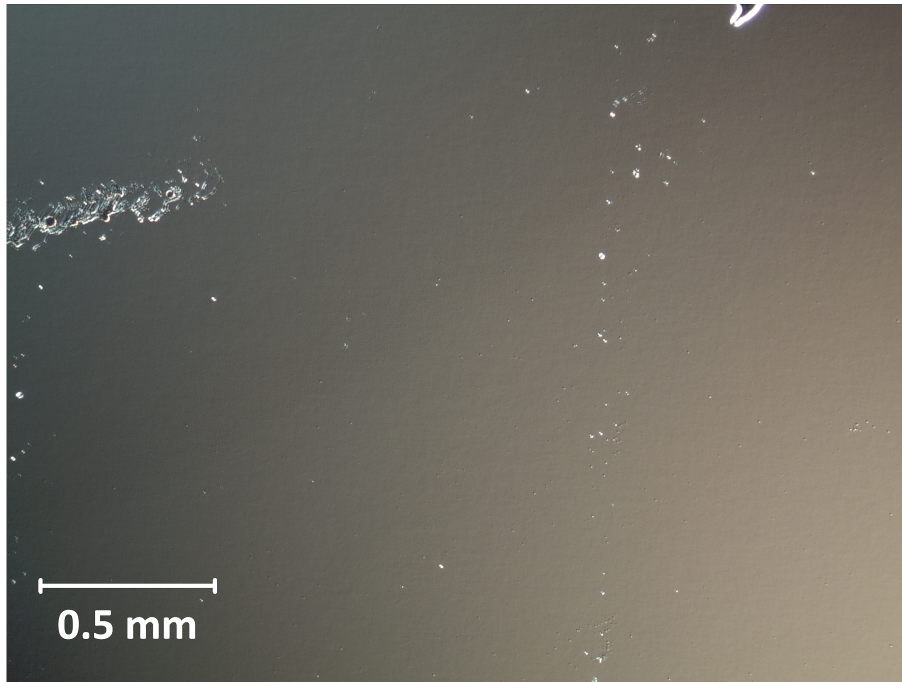

(A) Sample A Rough Area ×50

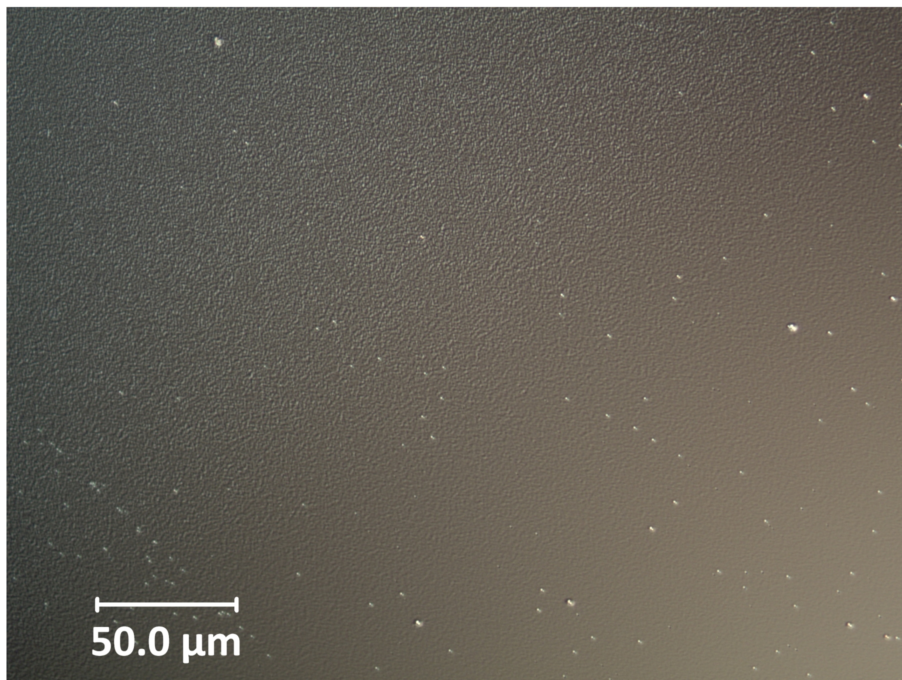

(B) Sample A Transition from Rough Area to Smooth Area. ×400

FIGURE 7.2: An example of a rough area under Nomarski for Sample A. The surface was rough at top-left of these two images and was smoother at bottom-right.

areas (see Fig 7.3). All of the bright rough areas were not covering up the full corner and usually leave a small margin to the wafer edge because the wafer holder blocks a small part of the edge of a quarter wafer. Molecular beams can only reach the unblocked area, where growth happens. The shiny group of dots on Sample A and B were defect groups, where defect sizes were large and often appear as holes under Nomarski microscopy.

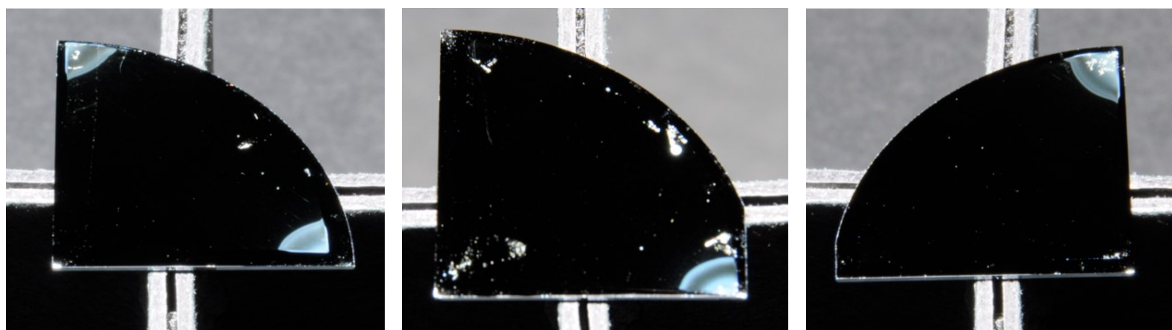

(A) Sample A Black Box Image (B) Sample B Black Box Image (C) Sample C Black Box Image

FIGURE 7.3: Comparison among black box images of the three wafer surfaces. Shiny points indicates defect spots. Bright rings indicates rough areas around the corners.

7.1.2 HRXRD Scanning Result

From the Nomarski images and the photos of the wafers, we can only infer that growth conditions were well optimized. We were to investigate the interfacial strain and that requires HRXRD scanning and fitting. The three samples were characterized by HRXRD using $\omega - 2\theta$ coupled scan in 004 reflection using a Jordan Valley QC3 HRXRD system. The dynamical XRD simulations were done using the RADS software package. The x-ray monochromator of CuKα_1 was used for all the three samples. The Bragg angle for the substrate reflection peak was 30.5687°. Therefore, the zero point of the $\omega - 2\theta$ angle on the x-axis in Fig 7.4 corresponds to 30.5687°. The scanning range for $\omega - 2\theta$ coupled scan was selected from -5000 to 5000 arcsec. The intensity of diffracted x-ray was relatively low and noisy for angles far from the substrate. Therefore, the scanning range of ±5000 was optimal. Fig 7.4 shows the high-resolution x-ray diffraction patterns for Sample A, B, and C, and the simulated InAs/AlSb structure with balanced interfacial strains (i.e. assuming no strained interfacial

layers between InAs and AlSb). The zero-order reflection peak position were found from optimized simulations using the Bragg equation $sin\theta = \frac{n\lambda}{2\langle a \rangle}$, where $\langle a \rangle$ was the weighted average lattice constant of the superlattice.

We traced the SL peaks of the same order, and it is seen that the tensile strain, resulting from unintentional displacement of Sb by As atoms, shifts the SL peaks to higher angles. This brings the 0th order reflection closer to the InAs substrate reflection, effectively helping to compensate compressive strain in the nominal AlSb barriers.

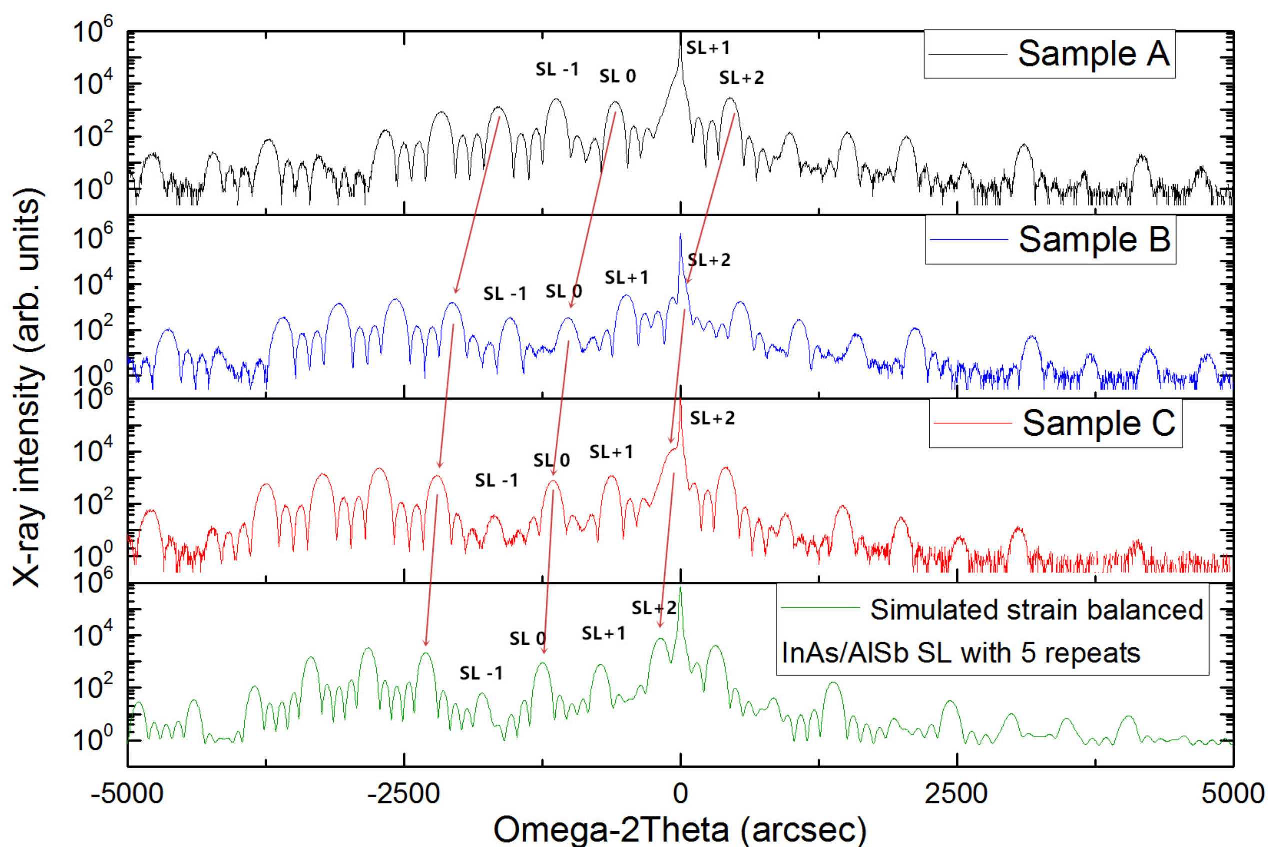

FIGURE 7.4: XRD scanning results and comparison among Sample A (black), B (blue) and C (red). Strain in the superlattice increases as the level of background As flux increases. The arrows map corresponding SL peaks.

As discussed in the previous section, the AlSb layers in Sample A were grown with a fully

opened As valve behind the closed shutter and were expected to have the largest excess of AlAs bonds at the InAs/AlSb interfaces and the highest As composition in what effectively were AlAsSb barriers. The amount of As displacing Sb at both InAs interfaces and AlAsSb barriers is expected to be reduced for Sample B because the As flux was reduced by 80% when depositing AlSb, as a result of partial valve closure. Finally, the peaks for Sample C, grown with fully closed As valve during AlSb deposition, are shifted to higher angles by only small amount compared to nominal InAs/AlSb structure below it, indicating that displacement of Sb by As was strongly reduced there. Nevertheless, this shows that even with the As valve fully closed during AlSb growth, some displacement of Sb by As may be happening at the InAs/AlSb interface or in the barrier layers, most likely as a result of a final time needed to close the As shutter.

The $\omega - 2\theta$ coupled scan probes a small 1D section of the 3D reciprocal space of the crystalline structure of our samples. Such reciprocal lattice is effectively a Fourier transform of the 3D electron distribution in the probed volume. The longer is such 1D scan in the reciprocal space, the finer is the probed volume in the real space. For the symmetrical 004 reflection such scan carries information about the lattice planes spacing along the growth direction. To obtain information about the average vertical strain in our superlattice, the scan needs to capture only the 0th order reflection and the main substrate peak. To gain quantitative information about the structure's period, the scan has to be at least of the length equals to the spacing between superlattice reflections, which in our case would require a scan range of about 550 arcsec. Since the scan range used in our experiments is equal to 10,000 arcsec, we expect it to give us an insight into the strain distribution in our structure with a resolution of about 20Å. This resolution is not sufficient to reveal the detailed strain distribution at the interfaces. However, based on the As bypass flux experiments described earlier, we know that this unintentional As incorporation will lead to an uniform tensile strain contribution in the barriers and an excess of AlAs bonds over InSb bonds at the InAs/AlSb interfaces. Consequently, in the dynamical XRD simulations discussed below, in order to obtain the best fit to the data, the only deviations from the nominal structure we considered is the fraction of AlAs bonds at the InAs/AlSb interface and the As content in the barrier.

7.2 XRD simulations

7.2.1 XRD fitting for As-induced strain

Based on the argument outlined above, for each of the three structures we assumed that the AlSb/InAs interface remained strain-balanced, while As displaced Sb from bonds only at InAs/AlSb interfaces and in AlSb barriers. The total surplus tensile strain caused by such displacement shifts the 0th order superlattice reflection to higher diffraction angles. In principle, the shift needed to align experimental and simulated diffractograms could be accomplished by assuming that As displaces Sb only at InAs/AlSb interfaces.

To test such scenario, we performed dynamical simulation for Sample A using one monolayer of $(AlAs)_x(InSb)_{1-x}$ at the InAs/AlSb interfaces. By setting the AlAs bond fraction x to 0.82, we were able align the SL reflection peaks, however, the peaks envelope, as shown in Fig 7.5, is incorrect. The intensities of simulated SL peaks are off by orders of magnitude from the HRXRD data. It is clear that HRXRD data could not be explained with the As displacing Sb only at InAs/AlSb interfaces. Attempts to distribute such excess of AlAs bonds between both InAs/AlSb and AlSb/InAs interfaces did not lead to a noticeable improvement, confirming the conclusion from our shutter bypass measurements that As must be also present in the nominally As-free barrier region.

Consequently, we tried to fit the HRXRD data with As incorporated AlSb layers and one As-rich interfacial monolayer. With As incorporated, $AlAs_ySb_{1-y}$ layers was used in the model to replace AlSb layers. Also, one monolayer of $(AlAs)_x(InSb)_{1-x}$ was used in the interface to provide better alignment for the SL peak envelopes.

Using this model after careful adjustment of excess As locations, excellent XRD fittings for all three samples could be obtained. The detailed structure of the simulated models are tabulated in Table 7.1, 7.2 and 7.3, for Sample A, B, and C, respectively. The comparisons between the actual data and simulated data are plotted in Figure 7.6a, 7.7a, and 7.8a, for Sample A, B, and C, respectively. The plots indicating a change in As composition are illustrated in Figure 7.6b, 7.7b, and 7.8b, for Sample A, B, and C, respectively.

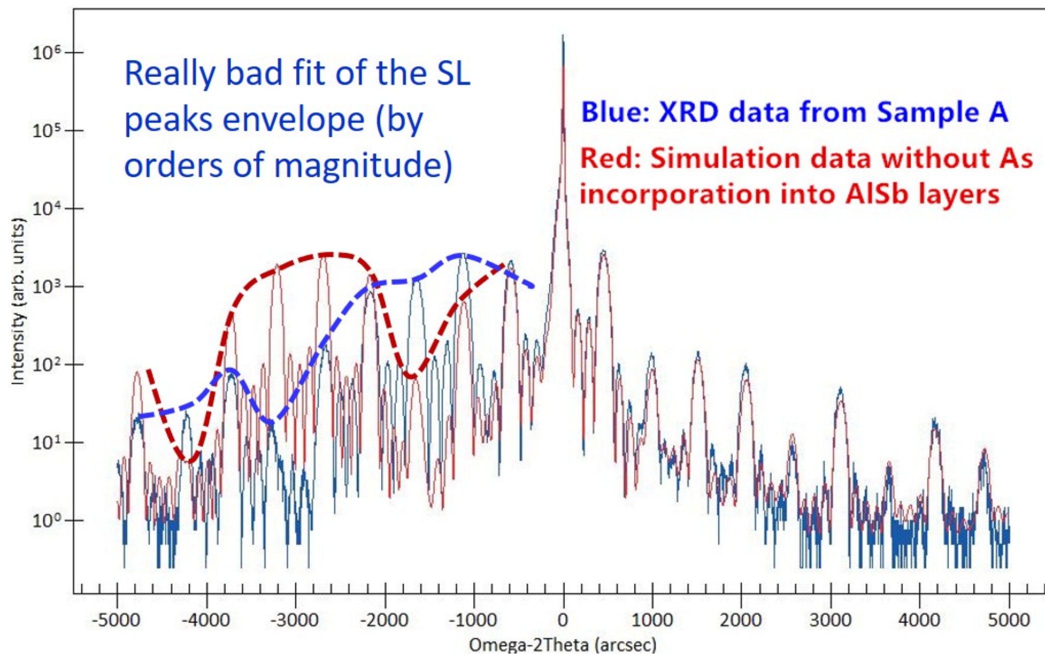

Figure 7.5: XRD dynamic simulation result for Sample A if extra As only existed at the interfaces. Not a good fit overall.

Material	Thickness	Repeat
$AlAs_{0.068}Sb_{0.932}$	145.13Å	5
$(AlAs)_{0.90}(InSb)_{0.10}$	2.87Å(1ML)	
InAs	202Å	
InAs	2000Å	1
InAs substrate	N/A	N/A

Table 7.1: XRD simulation structure for Sample A

Material	**Thickness**	**Repeat**
$AlAs_{0.014}Sb_{0.986}$	147.11Å	5
$(AlAs)_{0.85}(InSb)_{0.15}$	2.89Å(1ML)	
InAs	203Å	
InAs	2000Å	1
InAs substrate	N/A	N/A

TABLE 7.2: XRD simulation structure for Sample B

Material	**Thickness**	**Repeat**
AlSb	147.18Å	5
$(AlAs)_{0.76}(InSb)_{0.24}$	2.82Å(1ML)	
InAs	201Å	
InAs	2000Å	1
InAs substrate	N/A	N/A

TABLE 7.3: XRD simulation structure for Sample C

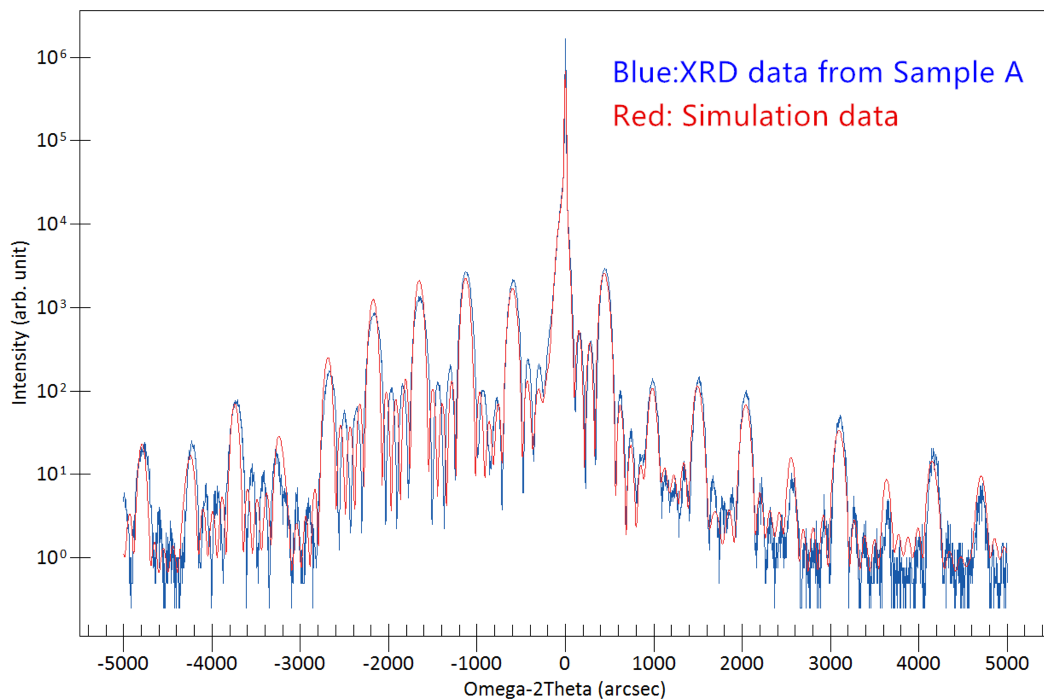

(A) XRD scan results of Sample A compared to simulation results. Blue: HRXRD scan result. Red: Simulated XRD data using Table 7.1

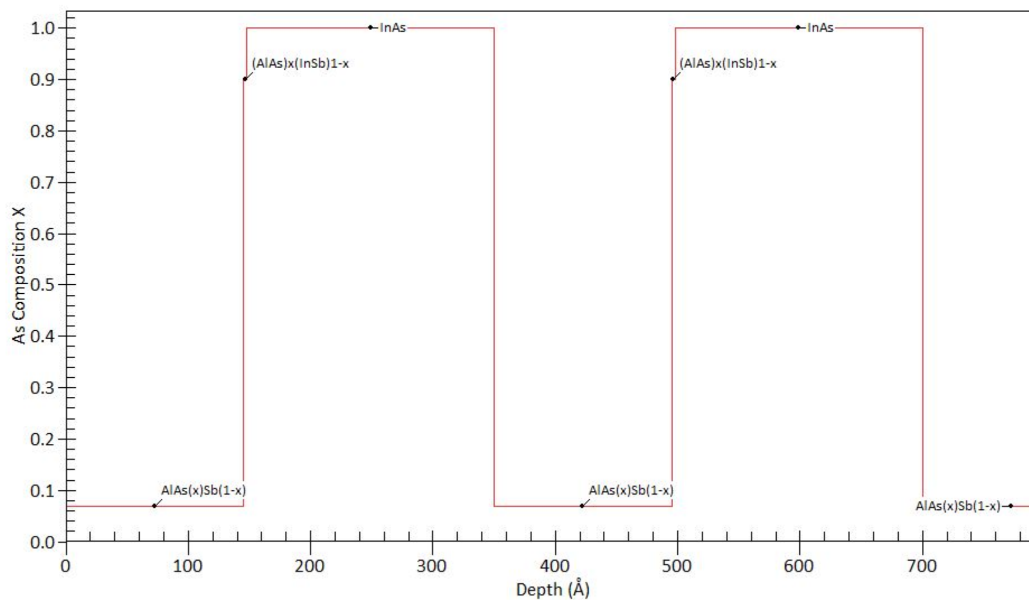

(B) As composition vs. layer thickness for Sample A

FIGURE 7.6: XRD fitting for Sample A and the As composition within the superattice

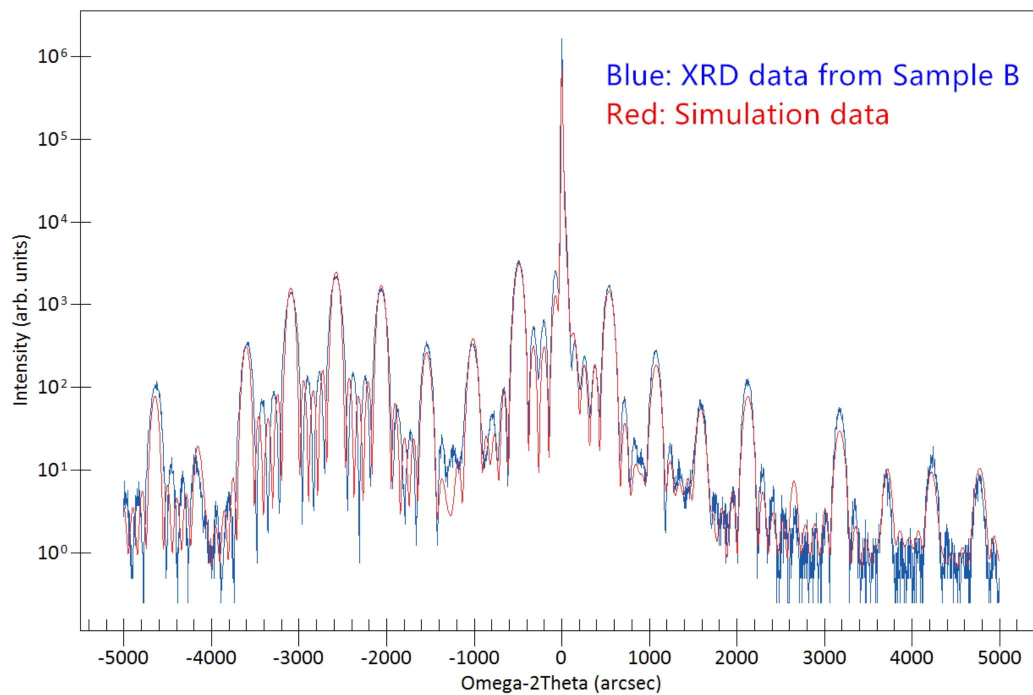

(A) XRD scan results of Sample B compared to simulation results. Blue: HRXRD scan result. Red: Simulated XRD data using Table 7.2

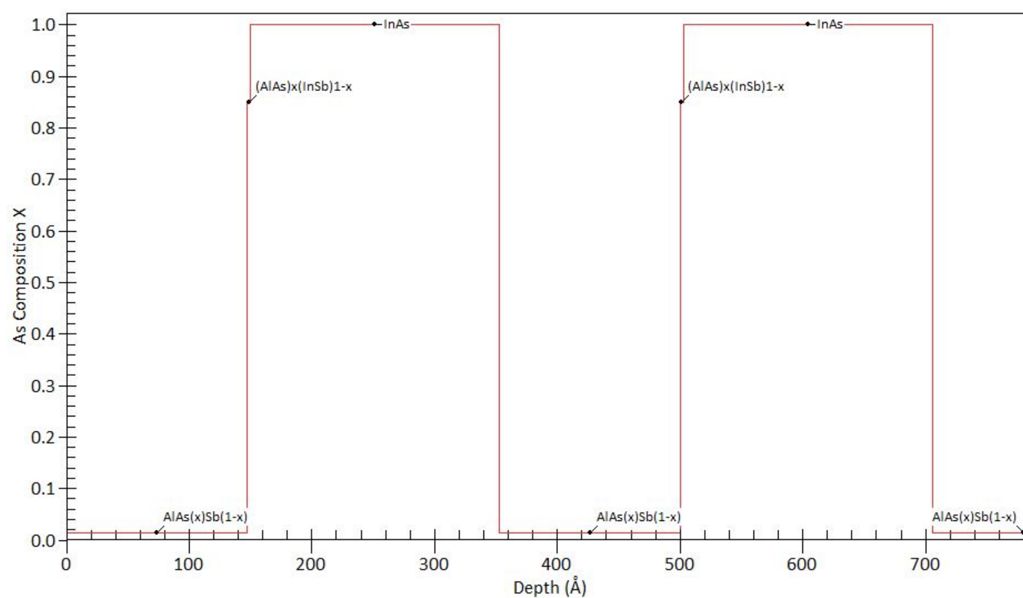

(B) As composition vs. layer thickness for Sample B

FIGURE 7.7: XRD fitting for Sample B and the As composition within the superattice

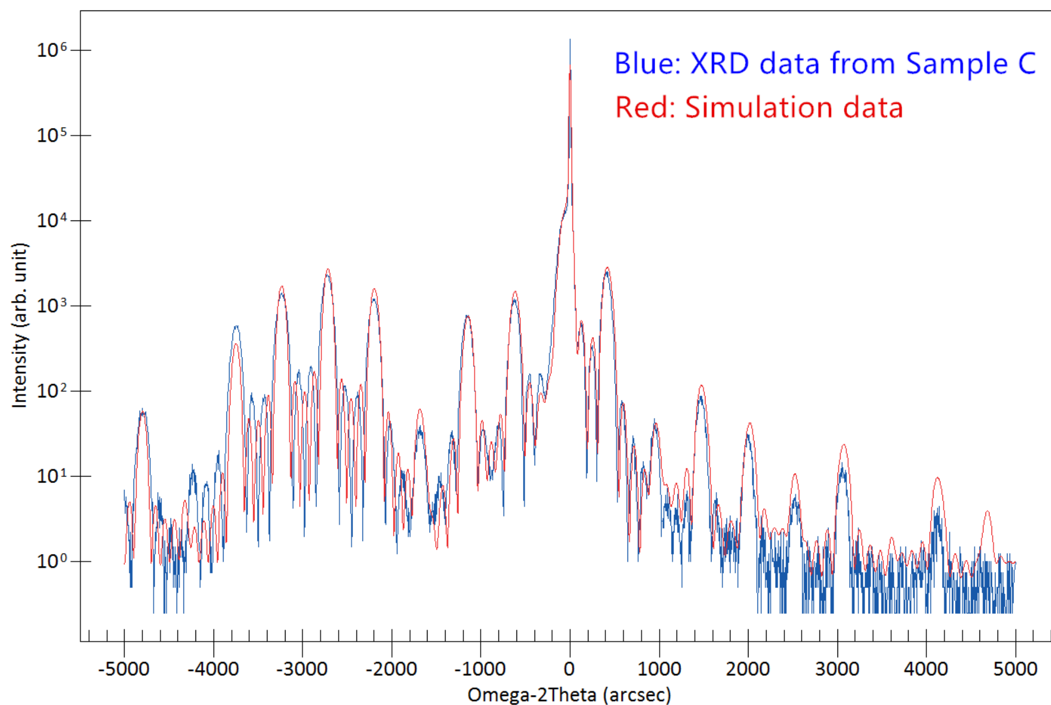

(A) XRD scan results of Sample C compared to simulation results. Blue: HRXRD scan result. Red: Simulated XRD data using Table 7.3

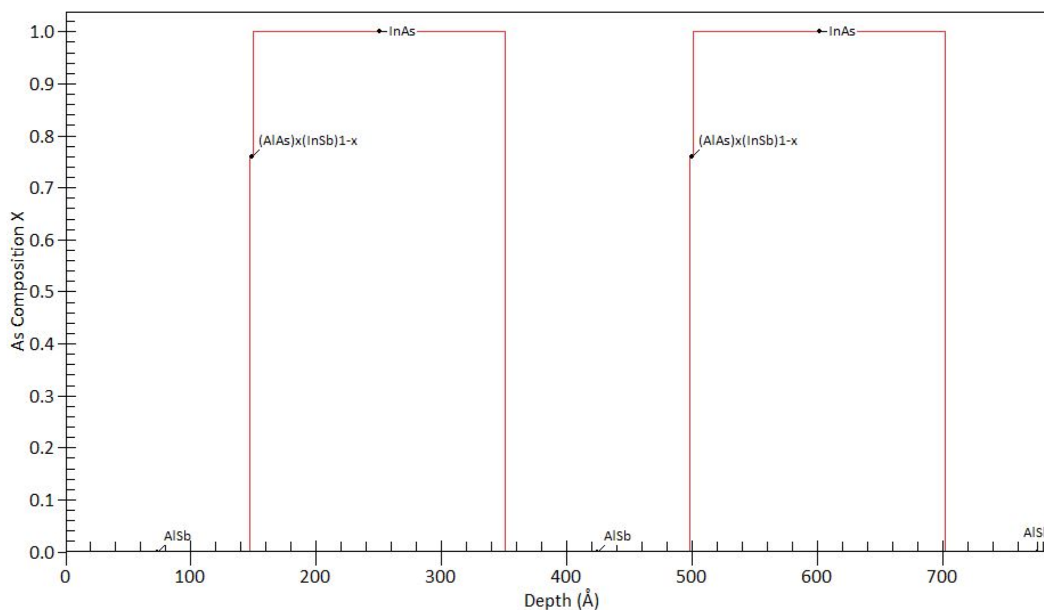

(B) As composition vs. layer thickness for Sample C

FIGURE 7.8: XRD fitting for Sample C and the As composition within the superattice

For Sample A, which used the conventional growth procedure with As valve open, the As was incorporated into the entire AlSb layer, forming $AlAs_{0.068}Sb_{0.932}$ even with the beam collimating shield in place. The unintentionally incorporated As composition is as high as 6.8%. Moreover, the interfacial monolayer between InAs and AlSb, $(AlAs)_{0.90}(InSb)_{0.10}$, was found to be almost entirely of Al-As character, with Al-As to In-Sb bond ratio of 9:1.

For Sample B, in which the As valve was lowered to the setting of 20% of its growth flux, a much smaller amount of As was incorporated within AlSb layers. The AlSb layers were found to be $AlAs_{0.014}Sb_{0.986}$, i.e. with unintentional As composition at 1.4%. The As composition for Sample B was 20.6% of that of Sample A. This is consistent with throttling of the As flux down to 20% during AlSb deposition.The interfacial monolayer was still As-rich but with slightly lower As content. The ratio between Al-As bond and In-Sb bond was 5.67:1.

For Sample C, no As was incorporated into the AlSb layers. However, the interface still needed to be As-rich to explain the total strain in the structure. Again, this was consistent with the observation of As flux presence after simultaneously closing As shutter and valve in the flux bypass experiment. Nonetheless, closing As valve along with the shutter effectively limited the As incorporation into AlSb layers.

The XRD fittings overall demonstrated well that even with the beam collimating shield in place, which reduces the As bouncing around in our MBE system, the As was unintentionally incorporated into the AlSb layers and InAs/AlSb interfaces. Arsenic flux bypass effect could be more significant for an MBE system without the beam collimation shield. This extra As was the cause of the excess strain in the superlattice structure. The HRXRD data from the three samples were well explained by optimized dynamical simulations.

7.2.2 Possible Exponential Decay Pattern for incorporated As within AlSb Layers

Recall that in Chapter 6.1, we hypothesized that the As might be incorporated within AlSb barriers, and decreases exponentially along the layer growth direction. For fitting the

XRD data of the three samples with graded layers, the lamellae function in the Jordan Valley RADS software was used. This function may separate one layer into a maximum of 200 individual layers; and if the layer was ternary or quaternary, the compositions of the elements could be defined to follow customized functions. For simulations including the As content exponential decay for the three samples, an exponential decay function was obtained from the second-stage mock recipe executions in section 6.2. Thereafter, we fitted the data for As_2 decay acquired by the oscilloscope, using a two-term exponential decay function. The fitting result for closing As shutter and leaving the valve open was plotted in Figure 7.9.

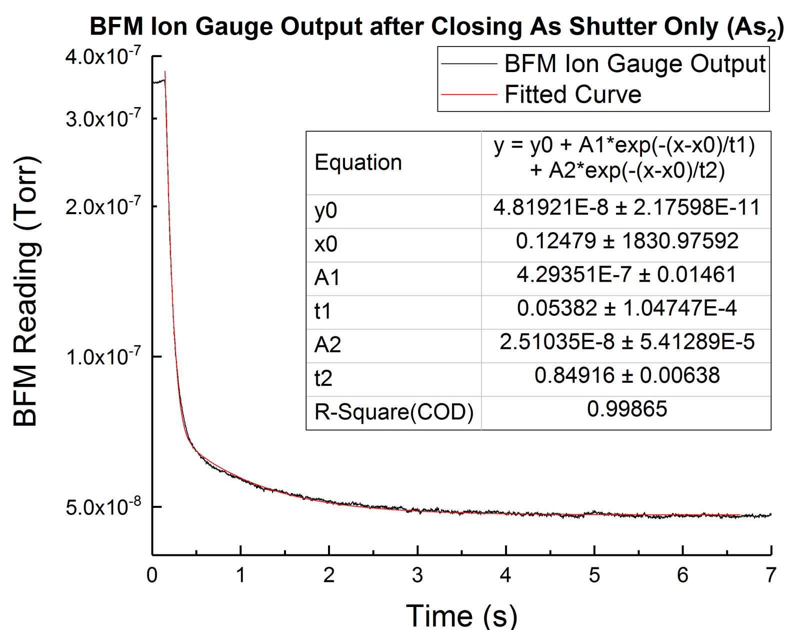

FIGURE 7.9: Fitting result of As exponential decay function for closed As shutter and open As valve, data acquired from the oscilloscope

From the fitting result, we converted the fitted function from beam equivalent pressure (BEP) vs. time to As composition y vs. relative thickness Z_r , assuming the growth rate of 1 Å/s and As composition in the $AlAs_ySb_{1-y}$ layers was proportional to the BFM readings. The As composition ranges from 0 to 1 and the relative thickness also ranges from 0 to 1. For instance, for a 150Å layer, the relative thickness Z_r at 150Å should be 1 and at 75Å should be 0.5. We assumed that the As incorporation rate was 1 Å/s because the In and Al

flux was set to grow at 1 Å/s for both InAs and AlSb growths. In this way, we obtained the relationship between the thickness of the AlSb layer and the As composition y for the case of As valve open and shutter closed (Sample A):

$$y = \exp(-414.9Z_r) + 0.0521\exp(-26.3Z_r) \tag{7.1}$$

where Z_r was in Å.

Material	**Thickness**	**As Composition**	**Repeat**
$AlAs_ySb_{1-y}$	145.13Å	Equation 7.2	5
$(AlAs)_{0.90}(InSb)_{0.10}$	2.87Å(1ML)	0.90	
InAs	202Å	1	
InAs	2000Å	1	1
InAs substrate	N/A	N/A	N/A

TABLE 7.4: XRD simulation structure with exponential decay As composition for Sample A

The two-term exponential decaying function would start from the As composition in the interfacial monolayer and end at the incorporated As composition in the barrier. In this case, the As variable composition y would follow Eq. 7.2 to decrease exponentially from 0.90 to 0.068. Therefore, for Sample A, we could get an excellent fit provided that we built the model as in Table 7.4, which was based on the model in Table 7.1. The adjusted two-term exponential decay function for As variable composition y has the form of:

$$y = \exp\left[-414.9Z_r + \ln(0.90)\right] + 0.0521\exp\left[-26.3Z_r + \ln(0.90)\right] + 0.068 \tag{7.2}$$

The ln term in this equation insured that the exponential decay of As composition would start from the As composition of the interfacial monolayer. The fitting result is plotted in Fig. 7.10

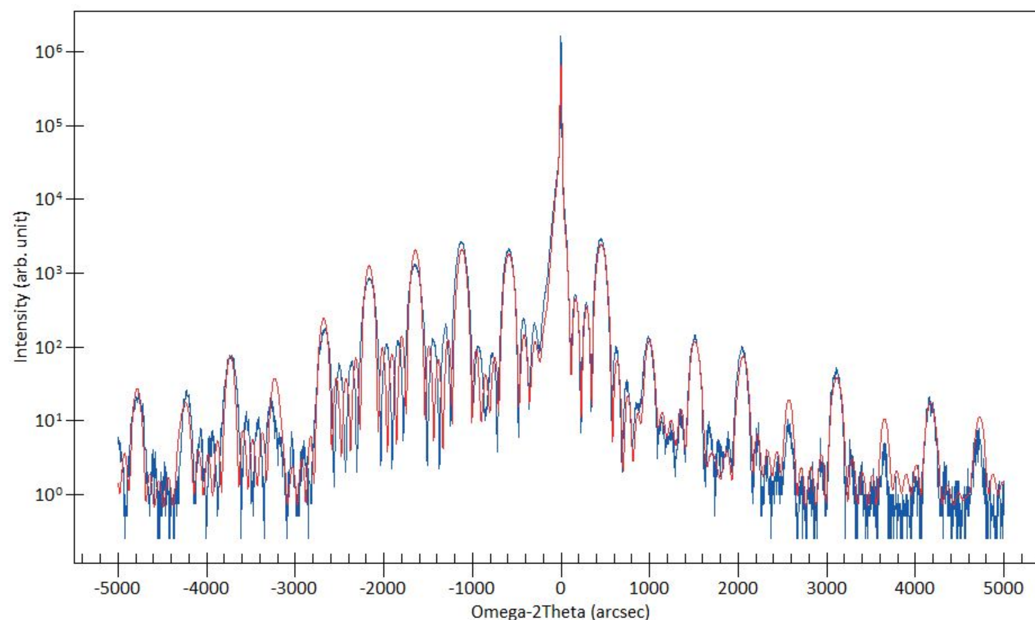

FIGURE 7.10: Sample A XRD simulation result with exponential decay As content within AlSb layers. Blue: Sample A HRXRD data. Red: XRD simulation data with exponential decay As content.

The XRD simulation with exponential decay As composition within AlSb layers have little or no difference visually comparing to the XRD simulation results with As abrupt drop in 7.6a. This was because the As content exponential decay was fast and only within the first few Ångstroms. Hence, the effect of adding small excess of strain resulting from the residual exponential decay of As in the structure was negligible.

We compared the XRD simulation model with exponential decay As composition in Table 7.4 to the model without exponential decay in Table 7.1. The simulation results of the two models are very close so that the graph needs to be zoomed in to distinguish each other. Therefore, the difference between the exponential decay and an abrupt drop in As composition is very small. Even if the As composition follows the exponential decay pattern, the decay was fast enough to be approximated as an abrupt drop. Therefore, neither could we conclude that the As in the first few monolayers of AlSb follows the exponential decay pattern, nor could we deny the possibility of the As composition decays exponentially instead of drops abruptly. The main reason to support the As exponential decay was that we

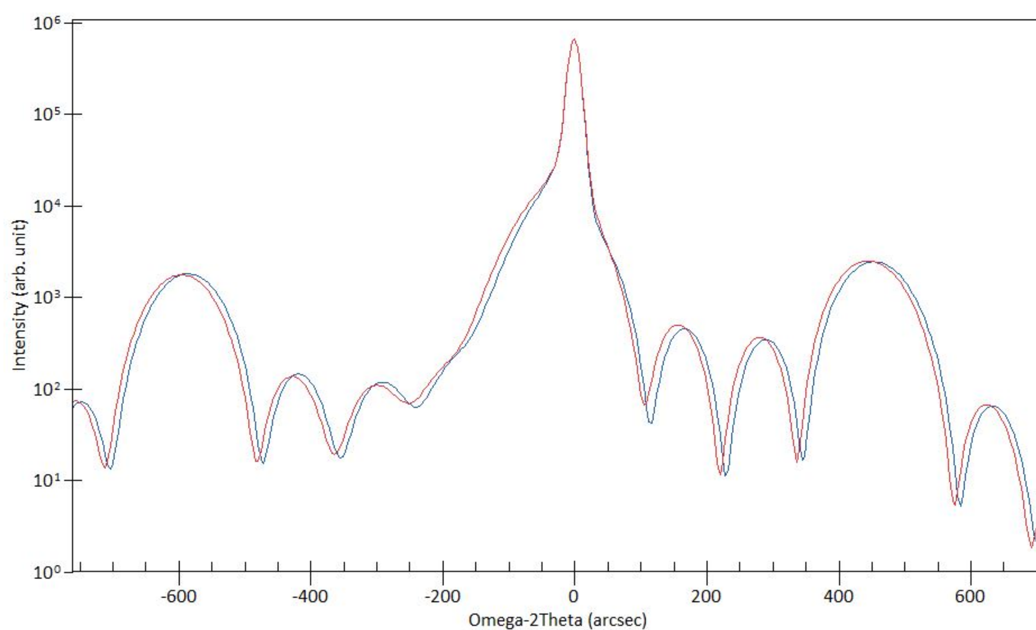

FIGURE 7.11: Sample A XRD simulation result with exponentially decay As content within AlSb layers comparing to an abrupt drop. Blue: XRD simulation model in Table 7.4 with As exponential decay in AlSb layers. Red: XRD simulation model in Table 7.1 with abrupt drop of As composition.

indeed observed this temporal behaviour after As shutter was closed. Albeit the effect was insignificant in our case, it is expected to be much more pronounced for most MBE systems, where As beam collimating apertures are not used.

Chapter 8

Conclusion and Future Works

Conclusion

In this thesis, the unintentional incorporation of As during the deposition of AlSb barriers in MBE-grown InAs/AlSb superlattices was investigated. The As molecular flux at the wafer position was tested using different As cell shutter - As cell valve configurations to simulate conditions subsequently employed during growth: : (**i**) both the As shutter and valve were open, (**ii**) the As shutter was closed but the valve was open, (**iii**) both the As shutter and valve were closed. It was found that closing the shutter only did not fully eliminate As flux from reaching the substrate and a steady-state As flux bypass of 11.2% was still present. On the other hand, closing both the shutter and the valve eliminated As flux at wafer position almost completely, leaving only 0.28% of the flux measured under scenario (**i**). The short-term As flux temporal dependence after shutter closure was also tested at the substrate position under the scenarios of (**ii**) and (**iii**). The As flux in both cases dropped abruptly to the value close to its steady bypass level within the first three seconds, i.e. the time needed to grow one monolayer of AlSb.

The effect of such As flux bypass on the strain distribution in InAs/AlSb superlattices was tested by growing three samples of nominally identical design, differing only by the setting of the As valve during deposition of AlSb barriers: settings as in (**ii**) and (**iii**) as wells as and intermediate setting between the two, with the As flux throttled to 20% of its value in **ii**). The results of high-resolution $\omega - 2\theta$ coupled scans at the 004 reflection were subsequently compared to dynamical simulations. Excellent agreement with the experimental data was obtained by incorporating the observations from the direct measurements of As bypass flux

into the simulations.

The summary and comparison among the three samples was tabulated in Table 8.1. The As flux temporal behavior suggest that some exponential decay of As content may be present in the AlSb barriers before a steady As content is reached. However, the magnitude of this effect is too small in our case to be confirmed by HRXRD experiments. We expect that such effect may be much stronger for MBE system which do not use As flux collimating apertures.

200Å/150Å InAs/AlSb SL with 5 repeats	**Sample A**	**Sample B**	**Sample C**
As valve setting when growing AlSb	Open	Lowered to the setting of 20% of flux during growth	Closed
Simulation results for the AlSb barriers	$AlAs_{0.068}Sb_{0.932}$	$AlAs_{0.014}Sb_{0.986}$	AlSb
InAs/AlSb interfacial monolayers	$(AlAs)_{0.90}(InSb)_{0.10}$	$(AlAs)_{0.85}(InSb)_{0.15}$	$(AlAs)_{0.76}(InSb)_{0.24}$

Table 8.1: Summary of growth and fitting results of Sample A, B, and C.

The key finding was that under typical scenario used for the growth of InAs/AlSb superlattices, where the As valve setting was not changed while switching from InAs to AlSb layer, significant displacement of Sb by As took place, converting the AlSb layer into $AlAs_{0.068}Sb_{0.932}$, i.e. a layer with arsenic content of close to 7%. Importantly, such strong effect was found in a system where special measures were taken to limit the As bypass effect by capping the As port with a tight flux collimating aperture. During the growth of InAs/AlSb QCLs such unintentional incorporation of As into AlSb barriers and InAs/AlSb interfaces plays a beneficial role of balancing the compressive strain in AlSb barriers, thus ensuring purely elastic distortions in the active region, without detrimental plastic relaxation. It is clear nevertheless that the conversion of AlSb barriers into $AlAs_xSb_{1-x}$ ternary

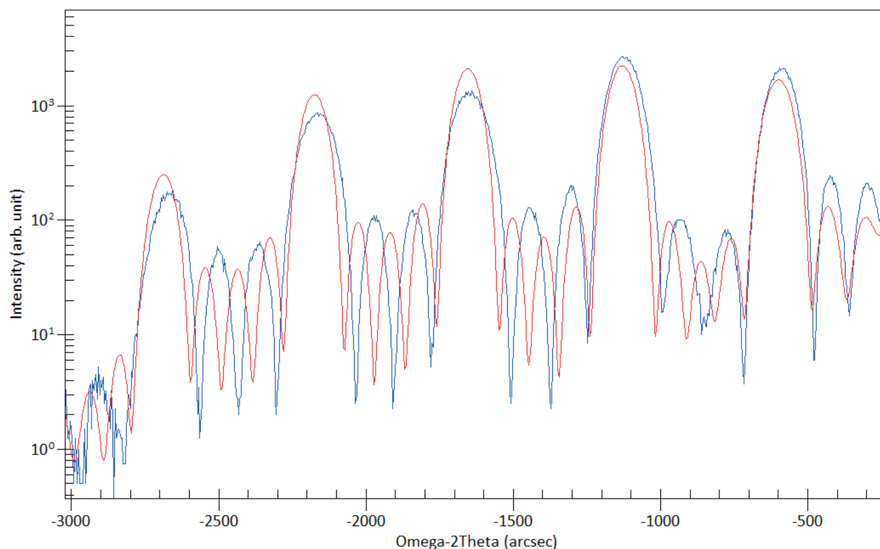

FIGURE 8.1: Comparison of Pendellösung fringes from XRD simulation for Sample B. Blue: HRXRD scan result. Red: Simulated XRD data.

alloy barriers would strongly influence the electronic levels in the active region as well as the electron tunneling probabilities. Incorporation of such effects into theoretical models may lead to further improvements in the performance of the InAs/AlSb - based devices.

Future Works

- Matching the Pendellösung fringes. Pendellösung fringes, which are interference fringes seen in between the superalltice reflections. Some discrepancy in these fringes positions is visible at larger distances to the left of the substrate peak. Taking Sample B simulation result for example, in Figure 8.1 between any two major peaks, three fringes were observed from the experimental data (blue), but only two fringes simulated (red).

- Further investigate the relationship between the amount of incorporated As and the residual As flux in the chamber. This may depend on the exact growth conditions. Indeed the growth condition dependent displacement of Sb by As was reported in [15].

Bibliography

[1] O Cathabard, R Teissier, J Devenson, J. Moreno, and A. Baranov, "Quantum cascade lasers emitting near 2.6 μ m", *Applied Physics Letters*, vol. 96, no. 14, p. 141 110, 2010.

[2] A. N. Baranov, M. Bahriz, and R. Teissier, "Room temperature continuous wave operation of inas-based quantum cascade lasers at 15 μm", *Optics express*, vol. 24, no. 16, pp. 18 799–18 806, 2016.

[3] Z Loghmari, M Bahriz, D. D. Thomas, A Meguekam, H. N. Van, R Teissier, and A. Baranov, "Room temperature continuous wave operation of inas/alsb-based quantum cascade laser at λ 11 μm", *Electronics Letters*, vol. 54, no. 17, pp. 1045–1047, 2018.

[4] J Devenson, R Teissier, O Cathabard, and A. Baranov, "Inas-based quantum-cascade lasers", in *Novel In-Plane Semiconductor Lasers VII*, International Society for Optics and Photonics, vol. 6909, 2008, 69090U.

[5] J Nicolai, C. Gatel, B Warot-Fonrose, R Teissier, A. Baranov, C Magen, and A Ponchet, "Elastic strains at interfaces in inas/alsb multilayer structures for quantum cascade lasers", *Applied Physics Letters*, vol. 104, no. 3, p. 031 907, 2014.

[6] J Nicolaï, B. Warot-Fonrose, C. Gatel, R Teissier, A. Baranov, C Magen, and A. Ponchet, "Formation of strained interfaces in alsb/inas multilayers grown by molecular beam epitaxy for quantum cascade lasers", *Journal of Applied Physics*, vol. 118, no. 3, p. 035 305, 2015.

[7] M. Vallet, Y. Claveau, B. Warot-Fonrose, C. Gatel, J. Nicolai, N. Combe, C Magen, R Teissier, A. Baranov, and A. Ponchet, "Highly strained alas-type interfaces in inas/alsb heterostructures", *Applied Physics Letters*, vol. 108, no. 21, p. 211 908, 2016.

[8] C. Kittel, P. McEuen, and P. McEuen, *Introduction to solid state physics*. Wiley New York, 1996, vol. 8.

[9] G. Burns, *Solid state physics*. Academic Press, New York, 1985, pp. 26–32.

[10] K. W. Kolasinski, *Surface science: Foundations of catalysis and nanoscience*. John Wiley & Sons, 2012.

[11] Z. Wasilewski, *Thin film analysis by x-ray scattering*, University of Waterloo Lecture Notes, 2018.

[12] X. Wang, "Inas/alsb based mid-infrared qcl growth and xrd simulation", Master's thesis, University of Waterloo, 2016.

[13] *Gen 10 mbe system manual*. Veeco Inc.

[14] Z. Wasilewski, *Semiconductor epitaxy: Driving fundamental discoveries and innovative applications*, Canadian Semiconductor Science and Technology Conference, 2015.

[15] T. Zederbauer, *Mixed group v compound semiconductors for intersubband devices*, eng. Wien, 2017. [Online]. Available: https://resolver.obvsg.at/urn:nbn:at:at-ubtuw:1-99046.

[16] M. A. Herman and H. Sitter, *Molecular beam epitaxy: Fundamentals and current status*. Springer Science & Business Media, 2012, vol. 7, pp. 6–12.

[17] Z. Wasilewski, *Research and monitoring tools: Ion gauges*, Molecular Beam Epitaxy Research Group of University of Waterloo QNC Webpage, 2014.

[18] *Granville-phillips series 274 bayard-alpert type ionization gauges manual*. MKS Instruments Inc.

[19] M. C. Tam, Y. Shi, D. Gosselink, M. Jaikissoon, and Z. R. Wasilewski, "Temperature monitoring of narrow bandgap semiconductors", *Journal of Vacuum Science & Technology B, Nanotechnology and Microelectronics: Materials, Processing, Measurement, and Phenomena*, vol. 35, no. 2, 02B102, 2017.

[20] A. Ichimiya, P. I. Cohen, and P. I. Cohen, *Reflection high-energy electron diffraction*. Cambridge University Press, 2004.

[21] S. Westcott, *Molecular beam epitaxy: Analysis techniques*, Rice University Lecture Notes CHEM 496.

[22] G. Nomarski, "Microinterféromètre différentiel à ondes polarisées", *J. Phys. Rad.*, vol. 16, 9S–13S, 1955.

[23] Z. Wasilewski, *Characterization tools: Nomarski microscopy*, Molecular Beam Epitaxy Research Group of University of Waterloo QNC Webpage, 2014.

[24] W. L. Bragg, "The diffraction of short electromagnetic waves by a crystal", 1929.

[25] B Lax, J. Mavroides, H. Zeiger, and R. Keyes, "Infrared magnetoreflection in bismuth. i. high fields", *Physical Review Letters*, vol. 5, no. 6, p. 241, 1960.

[26] R. N. Hall, G. E. Fenner, J. Kingsley, T. Soltys, and R. Carlson, "Coherent light emission from gaas junctions", *Physical Review Letters*, vol. 9, no. 9, p. 366, 1962.

[27] Z. I. Alferov, "Alas-gaas heterojunction injection lasers with a low room-temperature threshold", *Sov. Phys. Semicond.*, vol. 3, pp. 1107–1110, 1970.

[28] L. Esaki and R. Tsu, "Superlattice and negative differential conductivity in semiconductors", *IBM Journal of Research and Development*, vol. 14, no. 1, pp. 61–65, 1970.

[29] R. Kazarinov and R. Suris, "Electric and electromagnetic properties of semiconductors with a superlattice", *Soviet Physics Semiconductors-USSR*, vol. 6, no. 1, pp. 120–+, 1972.

[30] J. Faist, F. Capasso, D. L. Sivco, C. Sirtori, A. L. Hutchinson, and A. Y. Cho, "Quantum cascade laser", *Science*, vol. 264, no. 5158, pp. 553–556, 1994.

[31] J. Faist, F. Capasso, C. Sirtori, D. L. Sivco, J. N. Baillargeon, A. L. Hutchinson, S.-N. G. Chu, and A. Y. Cho, "High power mid-infrared λ 5 μm quantum cascade lasers operating above room temperature", *Applied Physics Letters*, vol. 68, no. 26, pp. 3680–3682, 1996.

[32] J. Faist, F. Capasso, D. L. Sivco, A. L. Hutchinson, S.-N. G. Chu, and A. Y. Cho, "Short wavelength λ 3.4 μ m quantum cascade laser based on strained compensated ingaas/alinas", *Applied Physics Letters*, vol. 72, no. 6, pp. 680–682, 1998.

[33] J. Faist, L. Ajili, G. Scalari, M. Giovannini, M. Beck, M. Rochat, H. Beere, A. G. Davies, E. H. Linfield, and D. Ritchie, "Terahertz quantum cascade lasers", *Philosophical Transactions of the Royal Society of London A: Mathematical, Physical and Engineering Sciences*, vol. 362, no. 1815, pp. 215–231, 2004.

[34] M. Beck, D. Hofstetter, T. Aellen, J. Faist, U. Oesterle, M. Ilegems, E. Gini, and H. Melchior, "Continuous wave operation of a mid-infrared semiconductor laser at room temperature", *Science*, vol. 295, no. 5553, pp. 301–305, 2002.

[35] C Becker, I Prevot, X Marcadet, B Vinter, and C Sirtori, "Inas/alsb quantum-cascade light-emitting devices in the 3–5 μm wavelength region", *Applied Physics Letters*, vol. 78, no. 8, pp. 1029–1031, 2001.

[36] C. Downs and T. E. Vandervelde, "Progress in infrared photodetectors since 2000", *Sensors*, vol. 13, no. 4, pp. 5054–5098, 2013.

[37] M. Brandstetter, M. A. Kainz, T. Zederbauer, M. Krall, S. Schönhuber, H. Detz, W. Schrenk, A. M. Andrews, G. Strasser, and K. Unterrainer, "Inas based terahertz quantum cascade lasers", *Applied Physics Letters*, vol. 108, no. 1, p. 011 109, 2016.

[38] R Teissier, D Barate, A Vicet, C Alibert, A. Baranov, X Marcadet, C Renard, M Garcia, C Sirtori, D Revin, *et al.*, "Room temperature operation of inas/ alsb quantum cascade lasers", *Applied physics letters*, vol. 85, no. 2, pp. 167–169, 2004.

[39] R Teissier, D Barate, A Vicet, D. Yarekha, C Alibert, A. Baranov, X Marcadet, M Garcia, and C Sirtori, "Inas/alsb quantum cascade lasers operating at 6.7μm", *Electronics letters*, vol. 39, no. 17, pp. 1252–1254, 2003.

[40] J Devenson, D Barate, R Teissier, and A. Baranov, "Short wavelength (λ= 3.5-3.65 μm) inas/alsb quantum cascade lasers", *Electronics Letters*, vol. 42, no. 22, pp. 1284–1285, 2006.

[41] J Devenson, O Cathabard, R Teissier, and A. Baranov, "In as/ al sb quantum cascade lasers emitting at 2.75–2.97 μ m", *Applied Physics Letters*, vol. 91, no. 25, p. 251 102, 2007.

[42] X. He, S. Wang, S. G. Razavipour, G. Liu, C. Xu, B. Wen, A. Mahmud, D. Gosselink, A. Tam, Z. R. Wasilewski, and D. Ban, "Characterization for mid-infrared quantum cascade lasers operating up to 350 k on pulse-mode", in *Canadian Semiconductor Science and Technology Conference*, 2017.

[43] J Spitzer, A Höpner, M Kuball, M Cardona, B Jenichen, H Neuroth, B Brar, and H Kroemer, "Influence of the interface composition of inas/alsb superlattices on their optical and structural properties", *Journal of applied physics*, vol. 77, no. 2, pp. 811–820, 1995.

[44] A Bauer, M Dallner, A Herrmann, T Lehnhardt, M Kamp, S Höfling, L Worschech, and A Forchel, "Atomic scale interface engineering for strain compensated epitaxially grown inas/alsb superlattices", *Nanotechnology*, vol. 21, no. 45, p. 455 603, 2010.

[45] Y. Claveau, M. Vallet, H. Tang, N. Combe, and A. Ponchet, "Elastic properties of alas-like and insb-like strained interfaces in [inas/alsb] heterostructures", *Applied Physics Letters*, vol. 109, no. 4, p. 041 903, 2016.